学位論文　（要約）

MULTIDIMENSIONAL QUANTITATIVE IMAGING OF TISSUE REGENERATION PROCESS IN CHRONICALLY INJURED MOUSE LIVER

(マウス肝臓の慢性障害時の組織再生過程の多次元定量画像解析)

平成２８年１２月　博士（理学）　申請

東京大学大学院理学系研究科

生物科学専攻

神元　健児

Table of contents

Abstract

The liver is known to have a high capacity to regenerate from various injuries. Hepatocytes are one of the two liver epithelial cell types and play central roles for various liver functions. Biliary epithelial cells (BECs) are another epithelial cell type, which also play significant roles for homeostasis. Upon liver injury these epithelial cells proliferate to repair the damaged liver. In chronically injured livers, BEC marker positive cells emerge and expand, and have been hypothesized to play a significant role in liver regeneration. The emergence of those BEC marker positive cells is also known as ductular reaction (DR). This dissertation aimed to reveal the mechanisms of DR and liver regeneration. Here, I show the three-dimensional (3D) structures and morphogenesis of the biliary epithelial tissue by developing multidimensional imaging methods to analyze their very complex structures. This dissertation consists of 2 parts. In chapter 1, by multidimensional imaging studies I show a new mathematic model that can explain the proliferation of biliary epithelial tissue quantitatively. In chapter 2, I describe the role of DR in liver regeneration. Based on experimental results in different injury models, I have proposed a new hypothesis that can explain the role of DR The hypothesis can also provide an explanation for the morphogenesis of complicated biliary structures. These results advance the understanding of the mechanisms of DR and liver regeneration.

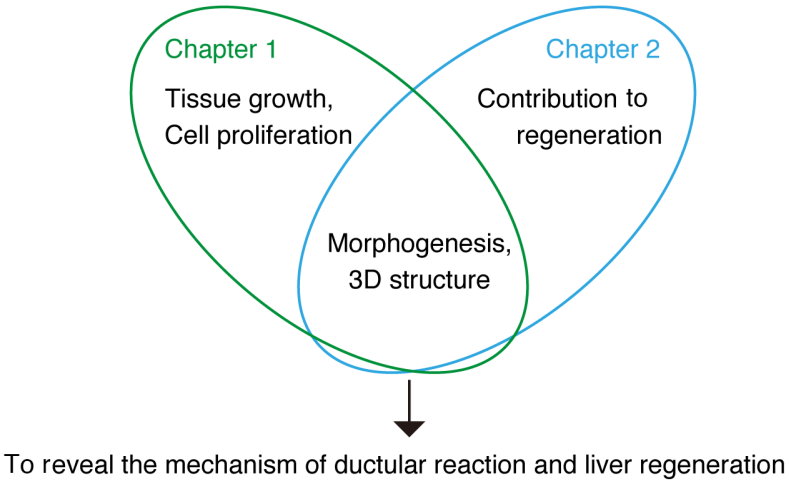

Figure 1. Aim and summary of this dissertation

Abstract of Chapter 1: Growth of biliary epithelial cells in injured liver

Dynamic remodeling of the intrahepatic biliary epithelial tissue is known to occur in liver regeneration, yet the cellular basis for this process remains unclear. Using unbiased approaches based on in vivo clonal labeling and tracking of biliary epithelial cells in the 3D landscape, in combination with mathematical simulation, I revealed their mode of proliferation in a mouse liver injury model. An apparent heterogeneity among biliary epithelial cells was observed. Upon liver injury, many BECs entered the cell cycle. While a majority of those cells exhibited a limited growth potential, a selected cell population continued to proliferate, contributing to expansion of the biliary trees. This study has highlighted a unique mode of epithelial tissue dynamics, i.e. it depends on the persistently proliferating cells that are maintained stochastically, but it does not depend on a hierarchical system driven by predetermined stem cells.

.

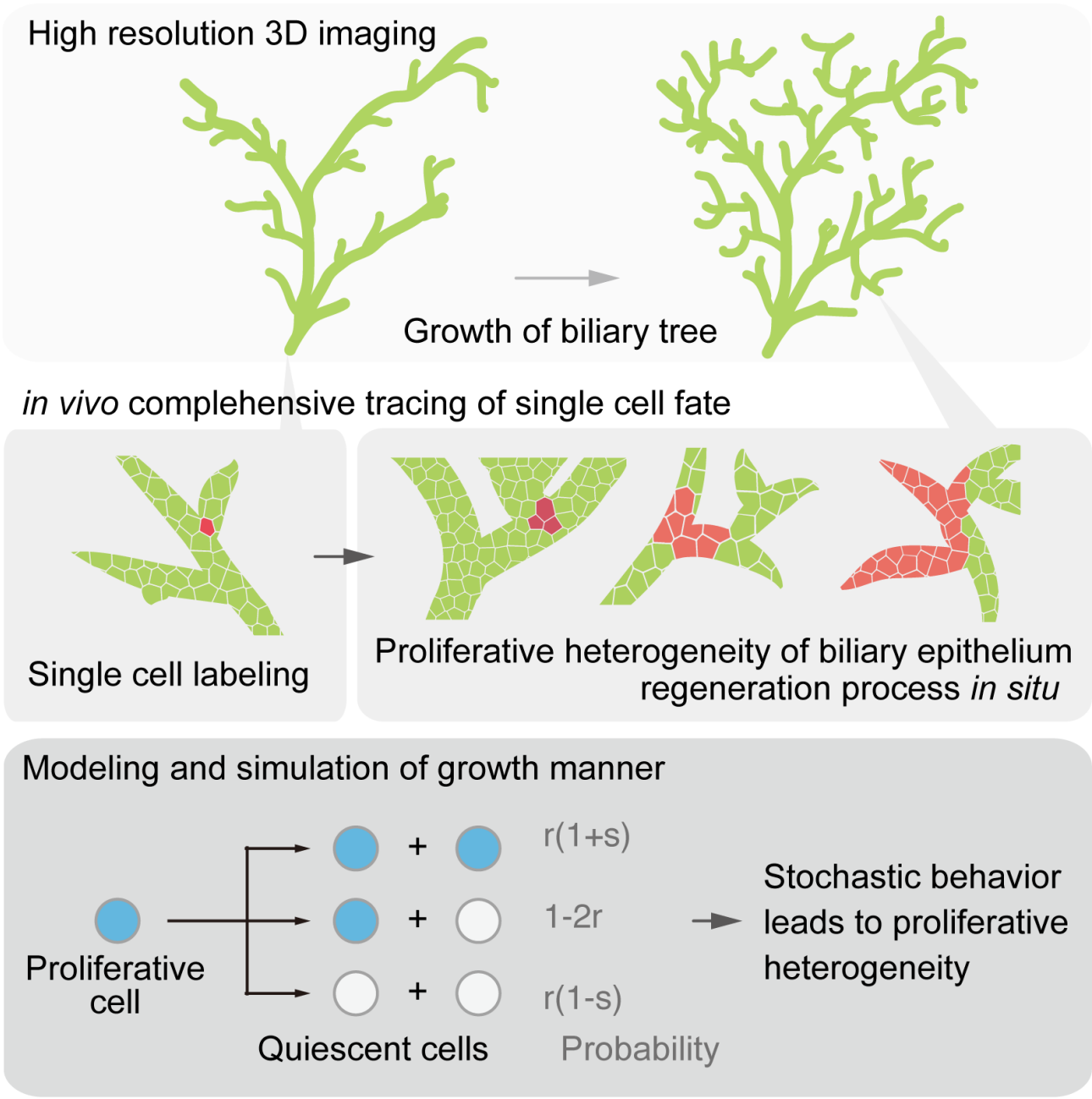

Figure 2. Graphical abstract (Chapter 1)

Abstract of Chapter 2: Role of ductular reaction in liver regeneration

本章については、５年以内に雑誌等で刊行予定のため、非公開。

Figure 3. Graphical abstract (Chapter 2)

Abbreviations

3D, three dimensional; AAT, Alpha-1 antitrypsin; AAV, adeno associated virus; APAP, acetaminophen; ApoE, Apolipoprotein E; BABB, benzyl-alcohol and benzyl-benzoate; BDL, bile duct ligation; BEC, biliary epithelial cell; BrdU, 5-bromo-2-deoxyuridine; CAG promoter, CMV early enhancer/chicken beta actin promoter; CCL4, carbon tetrachloride; CD, cluster of differentiation; CK19, cytokeratin 19; CLF, colyl lysyl fluorescein; CMFDA, 5-chloromethylfluorescein diacetate; CRISPR, clustered regularly interspaced short palindromic repeat; CV, central vein; Cas9, CRISPR associated proteins 9; DAPI, 4,6-diamidino-2-phenylindole; DDC, 3,5-diethoxycarbonyl-1,4-dihydrocollidine; DNA, deoxyribonucleic acid; DR, ductular reaction; ER, estrogen receptor; EdU, 5-ethynyl-2-deoxyuridine; EpCAM, Epithelial cell adhesion molecule; EtD-3, ethidium homodimer 3; FACS, fluorescence-activated cell sorting; FGF7, Fibroblast growth factor 7; FSC, forward scatter; GFP, green fluorescent protein; HGF, Hepatocyte growth factor; HTVi, hydrodynamic tail vein injection; IF, Immunofluorescent ; IFE, inter-follicular epidermis; KO, knock-out; LPC, liver stem/progenitor cell; LacZ, Bata galactosidase; MIP, maximum intensity projection; PBS, Phosphate buffered saline; PCR, polymerase chain reaction; PFA, paraformaldehyde; PV, portal vein; Prom1, prominin 1; R26R, Rosa 26 locus reporter; ROI, region of interest; ROS, reactive oxygen species; RT, room temperature; Rdx, Radixin; SD, standard deviation; SEM, standard error of the mean; SPP1, Secreted Phosphoprotein 1; SSC, side scatter; Sox9, SRY box 9; TAA, thioacetamide; TWEAK, TNF-related weak inducer of apoptosis; X-gal, 5-Bromo-4-chloro-3-indolyl-beta-D-galactopyranoside; bilPDs, biliary cell-derived proliferative ducts; c-Met, tyrosine-protein kinase Met; hepPDs, hepatocyte-derived proliferative ducts; iCre, improved Cre; indels, inserts or deletions; nLacZ, nuclear localization signal-conjugated LacZ; rAAV2/8, recombinant adeno-associated virus vector pseudo serotype with capsid 8; tdTomato, tandem dimer Tomato; vg, vector genome.

Chapter 1: Growth of biliary epithelial cells in injured liver

The results in Chapter 1 have been published in eLife (Kamimoto et al., 2016) and therefore quoted from this paper.

Introduction

Tissue growth, maintenance, and remodeling play central roles in ensuring the structural and functional integrity of adult organs and are achieved through the coordinated actions of cell proliferation and differentiation. In these processes, the location, arrangement and timing of cell proliferation are tightly regulated in tissue-specific and context-dependent manners (Barker et al., 2010). Selected and dedicated populations of adult stem cells that continuously provide progenies to replenish aged or damaged cells can be found in some tissues, while multiplication of differentiated cells also play an active role in normal tissue turnover and regeneration in other cases. Elucidating the mechanisms that regulate the spatiotemporal pattern of cell proliferation in intact tissues will provide fundamental insights into organ homeostasis and regeneration.

Functions and structures of the liver

The liver is a central organ for homeostasis exhibiting numerous functions, including various metabolic, synthetic and storage functions. It is also important that drug detoxification and synthesis of bile. The functions of the liver are associated with the blood circulation system and structures of the liver. The liver is connected to the intestine through the blood vessel, called portal vein (PV, **Figure 4A**). Blood from intestine enters the liver via the portal vein and drained from the central vein (CV). Between the PV and the CV, blood flows in the structure called sinusoid, which is the capillary vessel in the liver. As shown in **Figure 4B,** the liver consists of minimum unit structure called the hepatic lobule, in which the location of PVs forms hexagon like structure. Although the shape and appearance of hepatocytes may look uniform, they show different characteristics. Hepatocytes in the lobule are roughly divided into three types according to the location; zone 1 (area around PV), zone 2 (intermediate area between PV and CV), and zone 3 (area around CV). Hepatocyte shows different gene expression patterns according to these zonations.

Hepatocytes have the central role of the liver, and they are called as parenchymal cells. Hepatocytes are aligned in lines with sinusoids, which are shown as red in **Figure 4C**. Hepatocytes and BECs consist of epithelial cells in the liver. They have entirely different roles. However, at the developmental stage, they were originated from the same cell types, liver epithelial stem/progenitor cells (LPCs) (Miyajima et al., 2014; Tanimizu and Miyajima, 2007). After development, adult hepatocytes and BECs rarely divide.

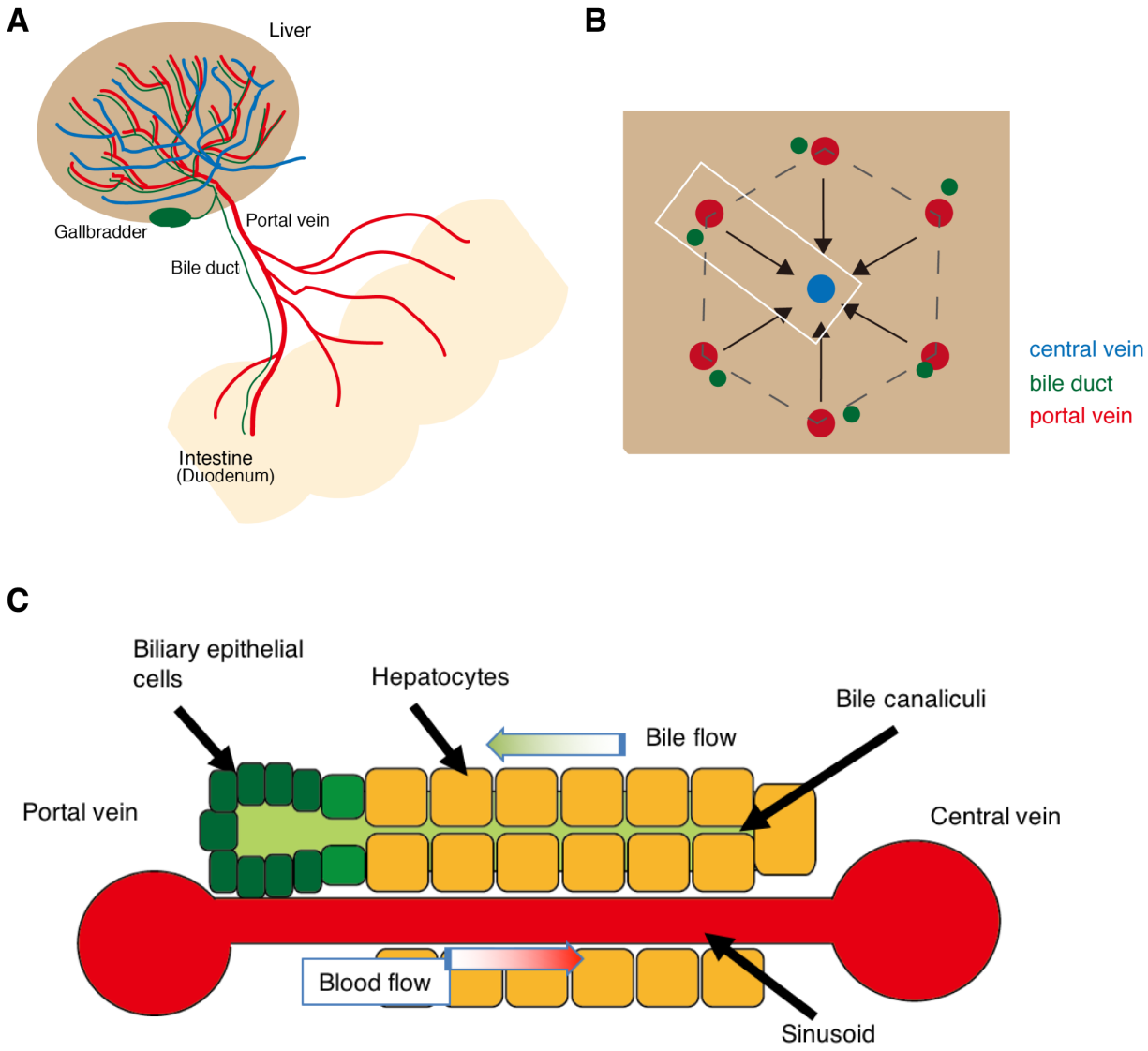

Figure 4. Structure of the liver (A) Macroscopic structure of the liver. Liver is connected to the intestine (duodenum). (B) The image shows the structures of sectioned liver tissue. Hepatic lobule is the minimum unit of liver structure. Black arrows indicate directions of blood flow. Hepatic artery is not shown. (C) Magnified image of liver structure, which is equivalent to the area surrounded by white box in (B).

Liver disease and regeneration

Liver epithelial cells are quiescent and rarely proliferate in normal conditions. However, once the liver is injured, hepatocytes show strong proliferative responses. In response to different insults, the liver regenerates by different mechanisms. In the case of surgical resection of 2/3 of liver mass, the remnant hepatocytes proliferate to restore the original liver mass in a few weeks in rodents (Miyaoka and Miyajima, 2013). In acute liver injury induced by a single injection of carbon tetrachloride (CCl_4), which is metabolized to toxic radicals by hepatocytes surrounding the CV, and injures those cells. Remained uninjured hepatocytes proliferate to recover the damage. In a chronic liver injury models, such as bile duct ligation, continuous administration of CCl_4, or continuous feeding of toxic drugs, damage hepatocytes continuously. In these chronically injured livers, DR is induced (Gouw et al., 2011).

DR and adult liver stem/progenitor cells

DR is histologically characterized as ectopic emergence and expansion of BEC marker-positive cells in the parenchymal region (**Figure 5**), and it has long been postulated that it represents the activation of adult LPCs that may reside in the biliary tree (**Figure 6**) (Grompe et al., 2009; Miyajima et al., 2014; Tanaka et al., 2011). Thus, along with DR in the chronic liver injury, BECs had been thought to give rise to new hepatocytes in the injured liver (**Figure 6**). Fundamentally, LPCs are defined as bi-potential proliferative cells that can differentiate to both hepatocytes and BECs. The concept of LPCs has been a paradigm in liver regeneration upon chronic injury, and most studies carried out so far have focused on whether and how LPCs can differentiate to hepatocytes to replenish the lost metabolic and synthetic functions of the liver.

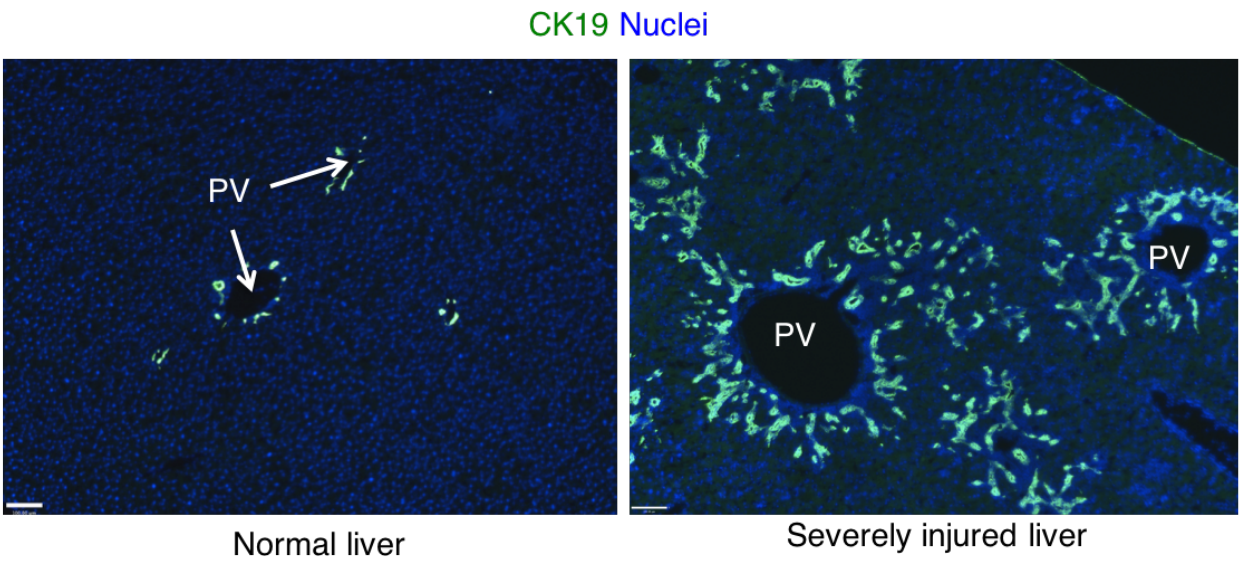

Figure 5. Representative image of DR. Immunohistochemistry of mouse liver sections in normal condition (the left panel) and in the chronically injured liver (DDC injury model, the right panel). CK19, which is a BEC marker gene, was visualized in green signal. Scale bar indicates 100 um.

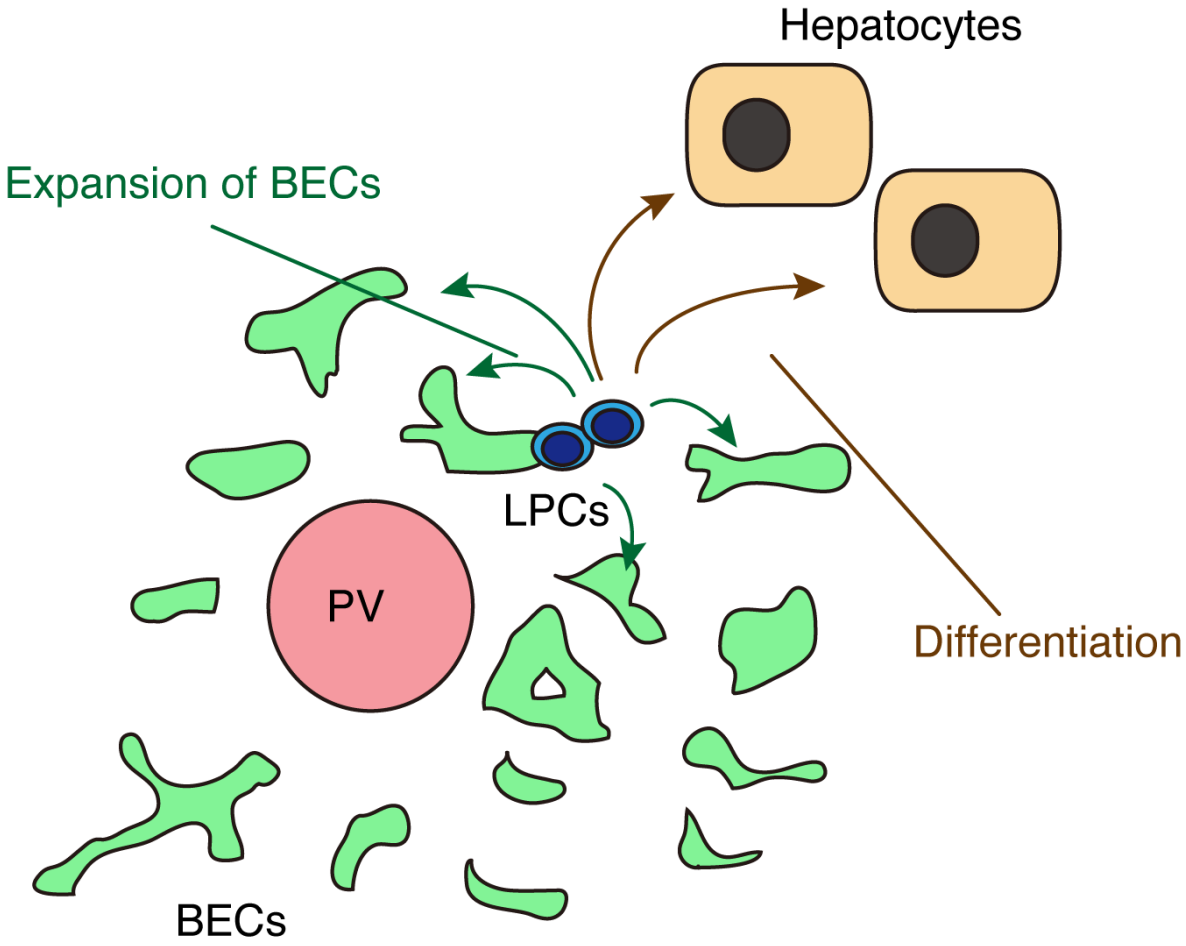

Figure 6. Schematic illustration of the activation of adult liver stem/progenitor cells (LPCs).

Contrary to a multitude of in vitro studies that have unequivocally demonstrated the presence of clonogenic and bi-potential LPCs in the biliary compartment (reviewed in : (Miyajima et al., 2014)), many recent studies employing genetic lineage tracing approaches in vivo have shown that LPCs and/or pre-existing BECs do not or rarely differentiate to new hepatocytes in mouse models, thereby casting doubt on the classic concept of LPCs serving as the stem/progenitor cells for hepatocyte regeneration under physiological conditions (Grompe, 2014; Tarlow et al., 2014; Yanger et al., 2014). Nevertheless, the pathophysiological relevance and functional importance of DR remain solid (Michalopoulos and Khan, 2015), as several lines of evidence involving knock-out mice for regulatory signals, such as TWEAK, HGF/c-Met and FGF7, have collectively demonstrated that suppression or failure of DR leads to exacerbated liver injury and severe defects in liver regeneration (Ishikawa et al., 2012; Lu et al., 2015; Takase et al., 2013). This means that although the role of DR is not fully explained by the stem/progenitor cell theory, DR is still necessary to liver regeneration, suggesting the existence of another important role.

Cell lineage tracing in mouse models

Many tools and methods have been developed to analyze cell lineages (Hsu, 2015; Kretzschmar and Watt, 2012). Among them, the Cre-loxP system is the most commonly used system for cell fate tracking in the mouse study (Branda and Dymecki, 2004). Cre is one of the DNA recombinases, and loxP is the target DNA sequence of Cre recombinase. Cre recombinase specifically recognizes loxP sequences and induces recombination between a pair of loxP sequences (**Figure 7**). This technology can be genetically encoded in mouse genome DNA.

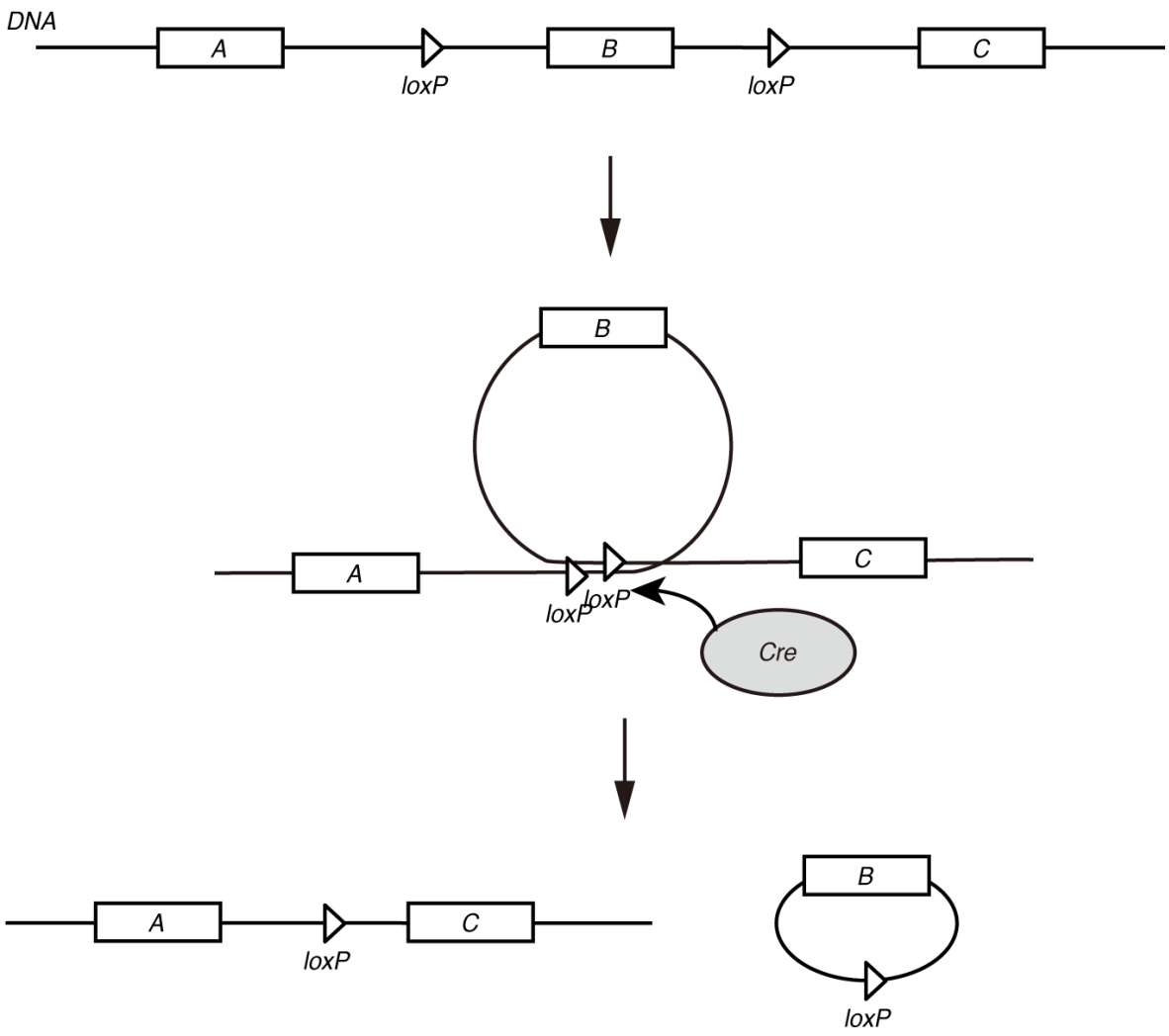

Figure 7. Schematic illustration of the Cre-loxP system.

By using the Cre-loxP system, we can permanently label the cell types of interest at any time, the fate of labeled cells can be traced. In many studies of lineage tracing, the inducible form of Cre, such as CreER, is used as described in **Figure 8**. CreER is a fusion protein of Cre with an estrogen receptor (ER) which becomes active only in the presence of tamoxifen. Activated CreER translocates into the nucleus and recombines target DNA. By adjusting the timing and dosage of tamoxifen administration, the timing and efficiency of DNA recombination can be set on demand. CreERT and CreERT2, which were used in this study, are modified versions of CreER.

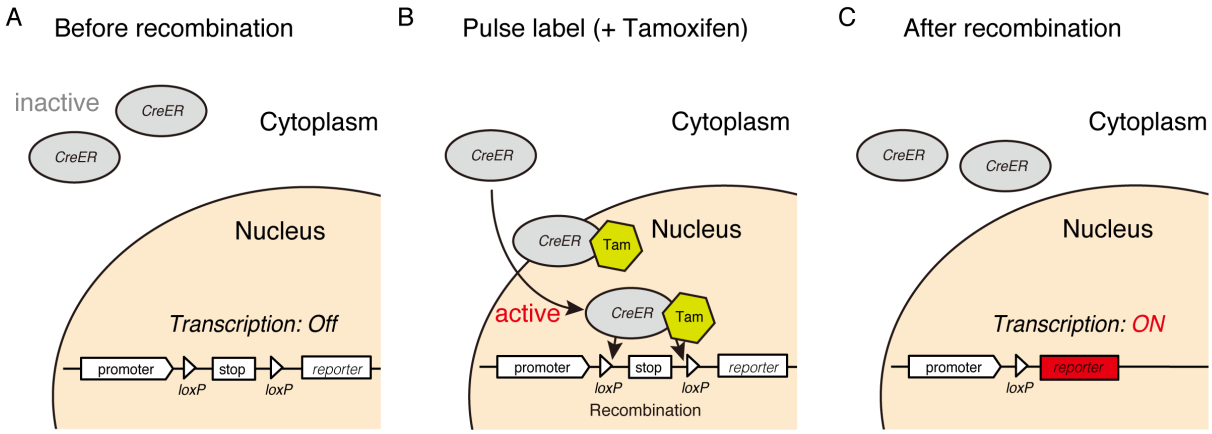

Figure 8. Pulse Cell labeling with CreER-loxP system. (**A**) CreER is expressed in specific cells of interest. CreER is inactive without tamoxifen. (**B**) By administration of tamoxifen, CreER is activated and relocates to the nucleus. In the nucleus, CreERT recombine loxP sequence, resulting in the loss of transcriptional stop sequence that blocks transcription of the reporter gene. (**C**) After recombination, transcription of the reporter gene will continue permanently. The recombination of DNA sequence remains in genome DNA and the cell labeling will continue in the daughter cells.

Origin of newly formed-biliary epithelial cells in injured liver

For many years, DR has been regarded and studied as a model that represents the activation of adult liver stem/progenitor cells which may reside in the biliary tree and can differentiate to hepatocytes and BECs (Grompe et al., 2009; Miyajima et al., 2014). Although in vitro studies have demonstrated the presence of clonogenic cells in the biliary compartment that are highly proliferative under culture conditions (Miyajima, Tanaka & Itoh, 2014), the in vivo existence and behavior of such proliferative BEC subpopulations remain unclear. This was partly because many recent studies employing genetic lineage tracing approaches in vivo were focusing on the trans-differentiation capacities between BECs and hepatocytes, rather than the mode of proliferation of BECs themselves (Grompe, 2014; Michalopoulos and Khan, 2015).

3D imaging of mouse organs

Using newly established imaging approaches to capture 3D tissue morphology, Kaneko et al have recently reported that DR observed in conventional histological analyses results from the dynamic and adaptive structural changes of the intra-hepatic biliary tree architecture (Kaneko et al., 2015). Thus, DR essentially represents drastic and complex remodeling of the biliary epithelial tissue, where a sophisticated mechanism that regulates the BEC proliferation is likely to be involved.

Single cell analysis and cellular heterogeneity

Recently, single cell approaches have been applied to the field of stem cell research (Etzrodt et al., 2014). Among these, in vivo quantitative single cell tracing has successfully revealed the presence of stem/progenitor cell populations and their unique features in various organs, providing fundamental insights into the cellular basis for tissue homeostasis, regeneration and tumorigenesis (Doupé et al., 2010; Driessens et al., 2012; Hara et al., 2014). This technique is designed to reveal a law of cellular dynamics underlying tissue growth by tracking a population of single cells comprehensively and deducing the characteristics of proliferative capacity, cell fate and behavior through statistical analyses involving mathematical simulation. A clonal cell tracing study on BECs was recently reported (Tarlow et al., 2014b), which focused solely on the clonal differentiation potential to both hepatocyte and BEC lineages, but not on the clone size representing the clonal growth potential. Thus, exact cell numbers of BEC-derived clones were not quantified. As the biliary

tree exhibits highly complex and fine structure (Kaneko et al., 2015), it is extremely difficult and practically unachievable to count or even estimate the number of BECs residing in it using conventional histological analysis in tissue sections. Hence, it is essential to develop a 3D imaging method to obtain detailed and reliable tissue structure images to perform quantitative assessment.

Stochastic behaviors in biology

In Chapter 1, I propose a computational model to recapitulate the experimental data of cell proliferation, and the model includes stochastic features. Many previous studies reported various kinds of the stochastic element in a variety of life events (Doupé et al., 2010; Hara et al., 2014; Kellogg and Tay, 2015; Samoilov et al., 2006). The stochastic feature is increasingly recognized nowadays. Even in the in vitro culture condition, where the environment is controlled to be homogeneous, the feature of the stochastic process was recognized (Kellogg and Tay, 2015; Tay et al., 2010).

In the cell fate decision and cell proliferation, stochastic property, randomness, and fluctuation are reported to exist in various tissues. In most cases, the cause of stochastic feature remains unclear, but the significance of it is increasingly recognized (Doupé et al., 2010; Driessens et al., 2012; Till et al., 1964).

Aims of this study

Here, I attempted to elucidate the basic mechanisms underlying the morphological transformation of the biliary tree, a key process involved in liver regeneration. In order to precisely understand the cellular dynamics in the context of complex tissue structures with branching morphology, I have developed new methods: high-resolution 3D imaging, quantitative single cell tracing, and computational simulation. Using this newly established platform for visualizing, labeling and tracing of BECs in liver tissue, I first revealed that expansion and remodeling of the biliary tree in a mouse model of chronic liver injury was predominantly driven by biliary epithelial tissue-intrinsic growth. Based on this experimental setting, I performed quantitative single cell tracing of BECs in vivo to elucidate the underlying cellular behavior, which was further characterized by mathematical modeling and computational simulation. The results highlighted hitherto unrecognized

heterogeneity among BECs and the mode of their proliferation, constituting the basis for the drastic and elusive structural transformation of the biliary epithelial tissue in regenerating liver in vivo.

Results

Ubiquitous and unbiased labeling of BECs using Prom1-CreERT2;R26R-tdTomato mice.

In order to achieve specific and permanent labeling of BECs, I employed a mouse strain where a tamoxifen-inducible variant of Cre, CreERT2 is knocked-in to the *Prominin1* (*Prom1*) locus, hereafter referred to as the Prom1-CreERT2 mouse (Zhu et al., 2009). While Prom1, better known as the surface antigen CD133, was reported to be an "oval cell/LPC marker" in injured liver (Dorrell et al., 2011; Rountree et al., 2007), it is also expressed in BECs under normal conditions (Suzuki et al., 2008). I examined the expression pattern of the endogenous Prom1 gene product in the normal adult mouse liver, and confirmed that it was expressed in essentially the same manner as CK19 and EpCAM, which are robust and reliable markers of BECs (**Figure 9**A, B).

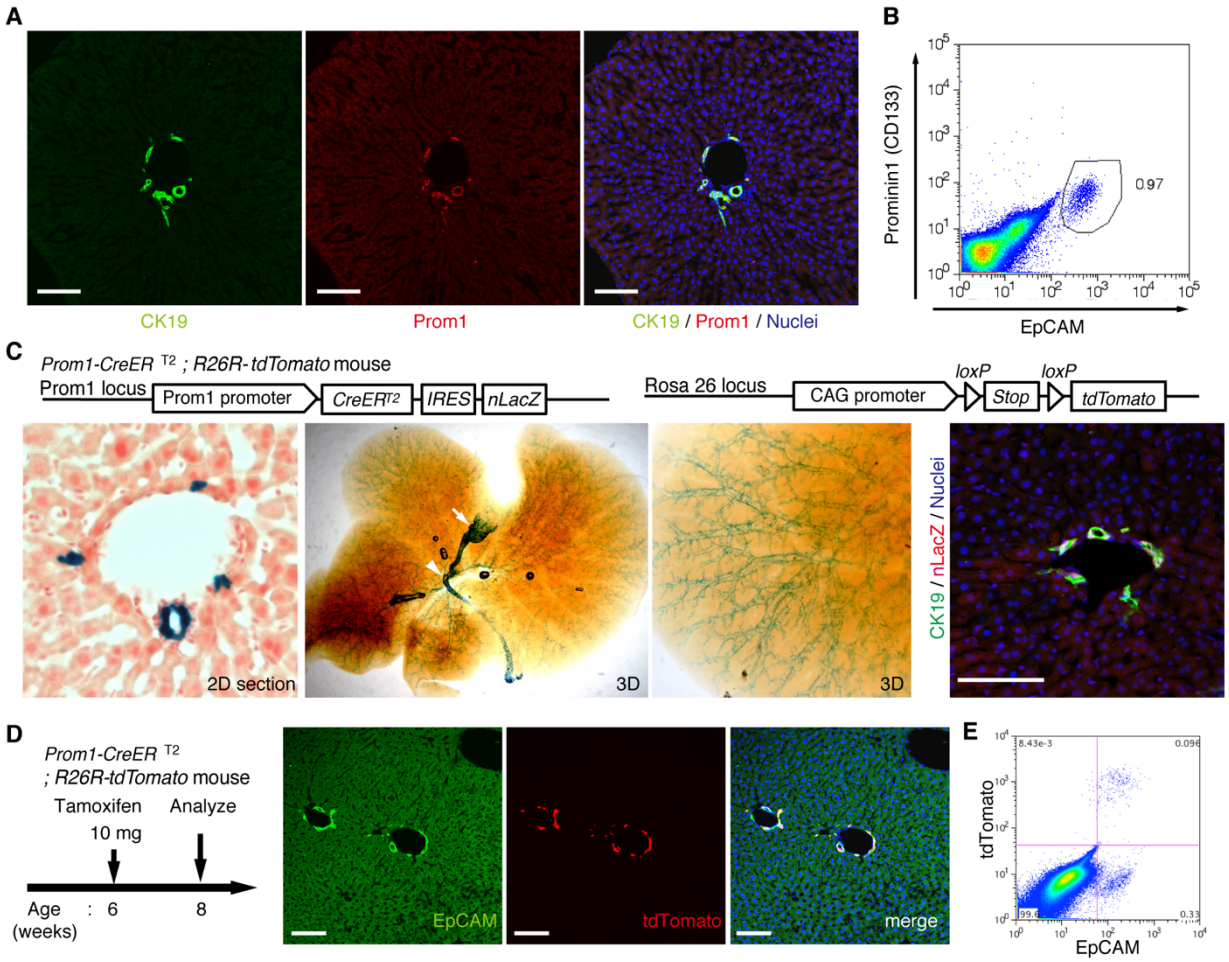

Figure 9. Visualization and lineage labeling of BECs using Prominin1 (Prom1) expression (**A**) Immunofluorescent (IF) staining for CK19 and Prom1 in the adult mouse liver (scale bars, 100 μm). (**B**) Representative expression pattern of Prom1 and EpCAM by fluorescence-activated cell sorting (FACS) analysis. Each dot or point represents an individual cell. The colors (pseudo-colors) indicate the density of dots (i.e., cells), corresponding to increasing numbers of events from blue to red. The outlying (and outlined) group highlights the EpCAM$^+$ Prom1$^+$ double positive population, indicating that these markers are co-expressed with each other. Successive gates were applied for DAPI$^-$, forward and side scatter (FSC/ SSC), and pulse width (not shown). (**C**) Prom1-CreERT2;R26R-tdTomato mice were used to allow the detection of Prom1$^+$ cells on the basis of LacZ expression. X-gal staining was performed on tissue sections (left panel) and whole liver samples (middle panels). The latter was cleared with benzyl-alcohol and benzyl-benzoate (BABB) after staining. The intra-hepatic biliary tree, as well as the extra-hepatic bile duct (white arrowhead), and the base of the gallbladder (white arrow) were visualized. Liver sections were also stained with anti-LacZ and anti-CK19 antibodies (right panel). (**D** and **E**) Lineage labeling in the

Prom1-CreERT2;R26R-tdTomato mouse liver after tamoxifen administration (scale bars, 100 μm). (**D**) Immunostaining of liver section. (**E**) Representative FACS plot pattern of labeled cells. Successive gates were applied for $DAPI^-$, FSC/SSC, pulse width and $EpCAM^+$ (not shown). All experiments were performed with at least 4 biological replicates.

In the Prom1-CreERT2 mice, the nuclear localization signal-conjugated LacZ (nLacZ) gene was also knocked-in to the same Prom1 locus. X-gal staining experiments using liver sections showed that nLacZ was expressed in a BEC specific manner (**Figure 9**C, left and right panels). I also performed whole-mount X-gal staining of the entire liver of the Prom1-CreERT2 mice. This resulted in 3D visualization of finely branching, tree-like architecture spreading throughout the organ (**Figure 9**C, middle and right panels), the pattern of which matches well with the biliary tree structure that was recently revealed by using an ink-casting technique (Kaneko et al., 2015). The staining pattern was also consistent with 3D images of CK19 immunostaining (see below).

I crossed the Prom1-CreERT2 mouse with a Cre-inducible fluorescent reporter mouse strain (R26R-tdTomato) for permanent labeling and tracing of BECs (Madisen et al., 2010). I first administered a relatively high dose of tamoxifen (10 mg/20 g mouse body weight) into Prom1-CreERT2;R26R-tdTomato mice and analyzed their livers to evaluate labeling specificity and efficiency. Immunostaining images (**Figure 9**D) and FACS plot (**Figure 9**E) showed that all the labeled cells were included in the $EpCAM^+$ BEC population, indicating that the Prom1-CreERT2;R26R-tdTomato mouse can be used for specific labeling of BECs. The labeling efficiency at this dose of tamoxifen was approximately 30% (**Figure 10**). The labeling seemed to occur at random in the BEC population, as the labeled $tdTomato^+$ cells were distributed ubiquitously among $EpCAM^+$ BECs with no apparent relation to features of the biliary structure, which will be described later in more detail. I also compared the Prom1-CreERT2 lineage-labeled and non-labeled cells in terms of their proliferative characteristics upon liver injury by 5-ethynyl-2'-deoxyuridine (EdU) incorporation assay and found no significant difference between them (**Figure 11**), showing that their proliferative capacities are indistinguishable. In addition, the BEC lineage labeling rate of around 30% did not change significantly even after DR was induced by a chronic injury model (**Figure 10**). I also confirmed that no leakiness of labeling occurred in the absence of tamoxifen administration (**Figure 12**). These results indicate that the BEC labeling in this system occurs in an un-biased manner, and the labeled cells faithfully represent the entire BEC population.

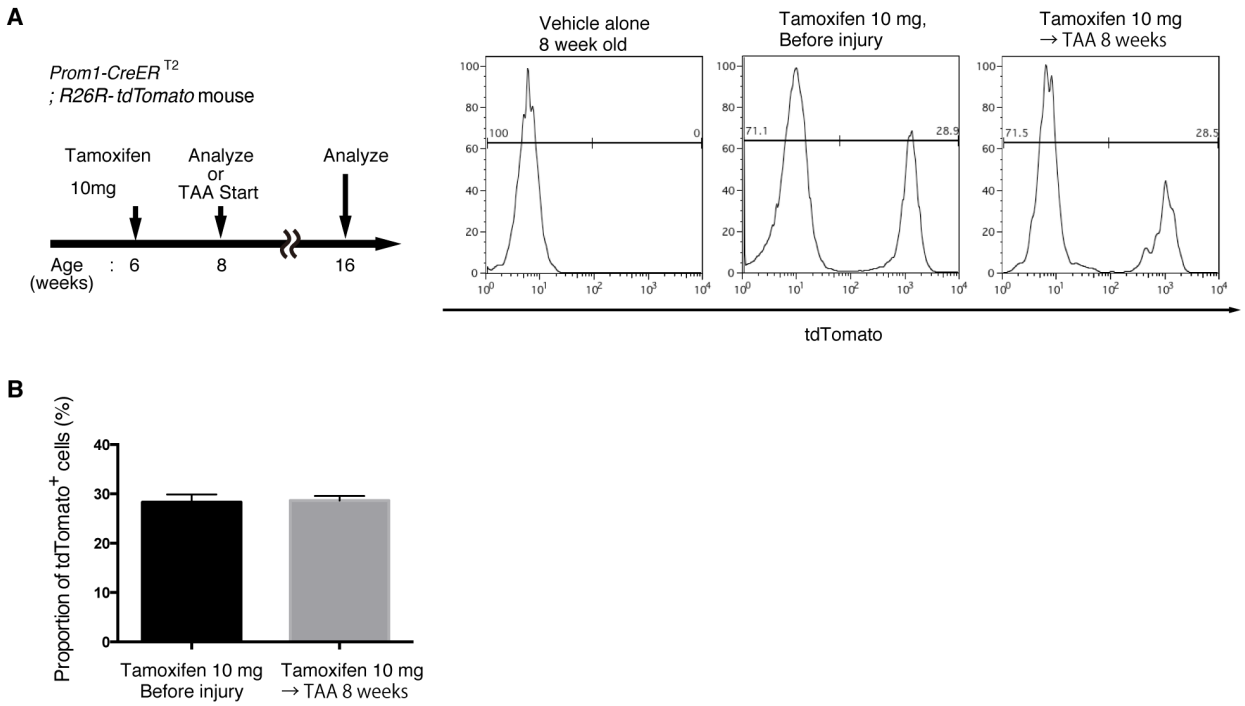

Figure 10. Quantification of lineage-labeled cells (**A**) BEC labeling ratio in the Prom1-CreERT2;R26R-tdTomato mice was evaluated by FACS analysis. Left panel shows the experimental design. 2 weeks after tamoxifen administration, the mice were subjected to analysis either directly (Before injury) or after 8 weeks of thioacetamide (TAA) injury. Non-parenchymal cells were collected from the dissociated liver and stained with anti-EpCAM antibody. FACS gates were applied sequentially as follows: $DAPI^-$ (live cells), FSC and SSC, pulse width, and $EpCAM^+$. No labeled cell was detected in the mice treated with vehicle alone (No tamoxifen). Before and after tamoxifen administration, $tdTomato^+$ cells were detected only in the $EpCAM^+$ population (not shown). (**B**) Quantification of the labeled BEC populations. No significant difference was observed between those before and after the TAA injury. The data represent the mean ± SEM for the results of five different experiments for each condition. $p = 0.70$ (un-paired Student's t-test).

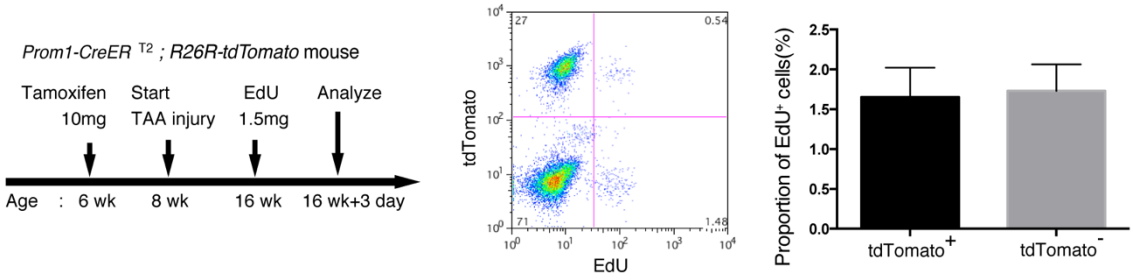

Figure 11. EdU uptake assay in lineage-labeled cells in Prom1-CreERT2;R26R-tdTomato mice. EdU uptake assay was performed to examine the proliferative characteristics of lineage-labeled and non-labeled BECs. After tamoxifen administration (10 mg/20 g body weight), the Prom1-CreERT2;R26R-tdTomato mice were subjected to TAA injury for 8 weeks, injected intraperitoneally with EdU (1.5 mg/20 g body weight), and then analyzed. For FACS analysis, successive gates were applied for $DAPI^-$, FSC/SSC, pulse width, and $EpCAM^+$ (not shown). No significant difference was observed between the labeled ($tdTomato^+$) and non-labeled ($tdTomato^-$) BECs. The data represent the mean ± SD for five mice each. $p = 0.58$ (paired Student's t-test).

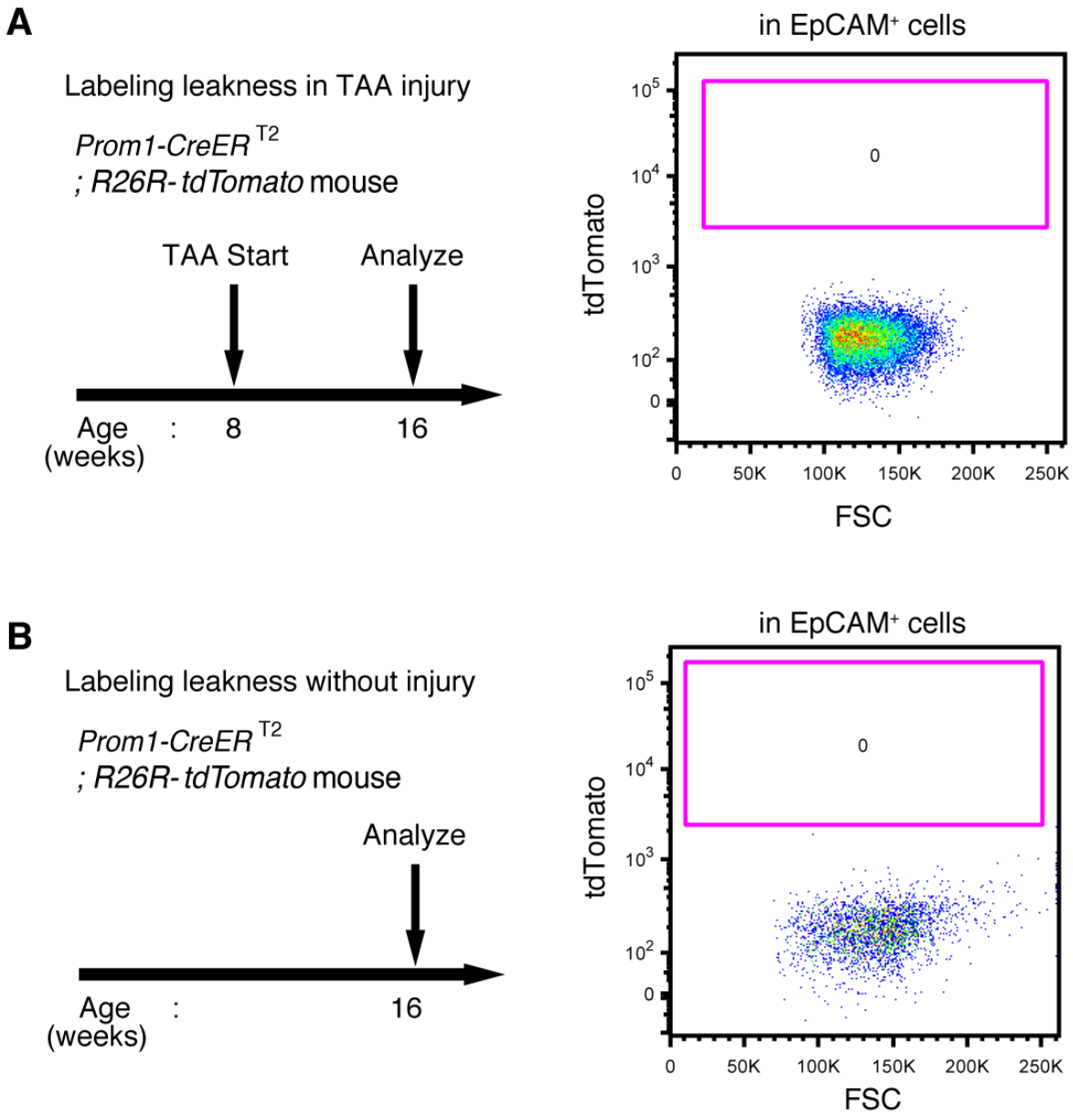

Figure 12. No labeled cells were detected in the absence of tamoxifen in Prom1-CreERT2;R26R-tdTomato mice. (**A** and **B**) Leaky labeling in the Prom1-CreERT2;R26R-tdTomato mice was evaluated by FACS analysis. Left panel shows the experimental design. The mice were analyzed in the presence (**A**) or absence (**B**) of TAA injury after 8 weeks. Non-parenchymal cells were collected from the dissociated liver and stained with anti-EpCAM antibody. FACS gates were applied sequentially as follows: $DAPI^-$ (live cells), FSC/SSC, pulse width, and $EpCAM^+$. No labeled cell was detected in either condition. Experiments were performed with three biological replicates and representative results are shown.

3D fluorescent imaging of the biliary tree with single cell resolution.

As shown in **Figure 9**C, the intrahepatic biliary epithelial tissue exhibits a complex yet ordered tree-like structure, which cannot be readily recognized by conventional histological analyses with thin tissue sections. I modified and improved a 3D immunostaining and imaging protocol using thick sections that was recently reported (Kaneko et al., 2015) and herein established a new fluorescent 3D imaging platform with a single-cell resolution. As schematically depicted in **Figure 13**A, I cut liver samples into thick sections (200 μm-500 μm thickness), followed by immunostaining and optical clearing. The 3D image obtained by this method recapitulated the basic structural unit of the biliary tree, consistently with those obtained by other protocols (Kaneko et al., 2015; Takashima et al., 2015) (**Figure 13**B); one or two duct tubes run along with the portal vein (PV) (**Figure 13**B; PV is not shown), and many finer branches, which I call ductules hereafter, protrude from the duct and wrap around the PV (**Figure 13**C). This structural unit was observed around the entire biliary tree (**Figure 15**A).

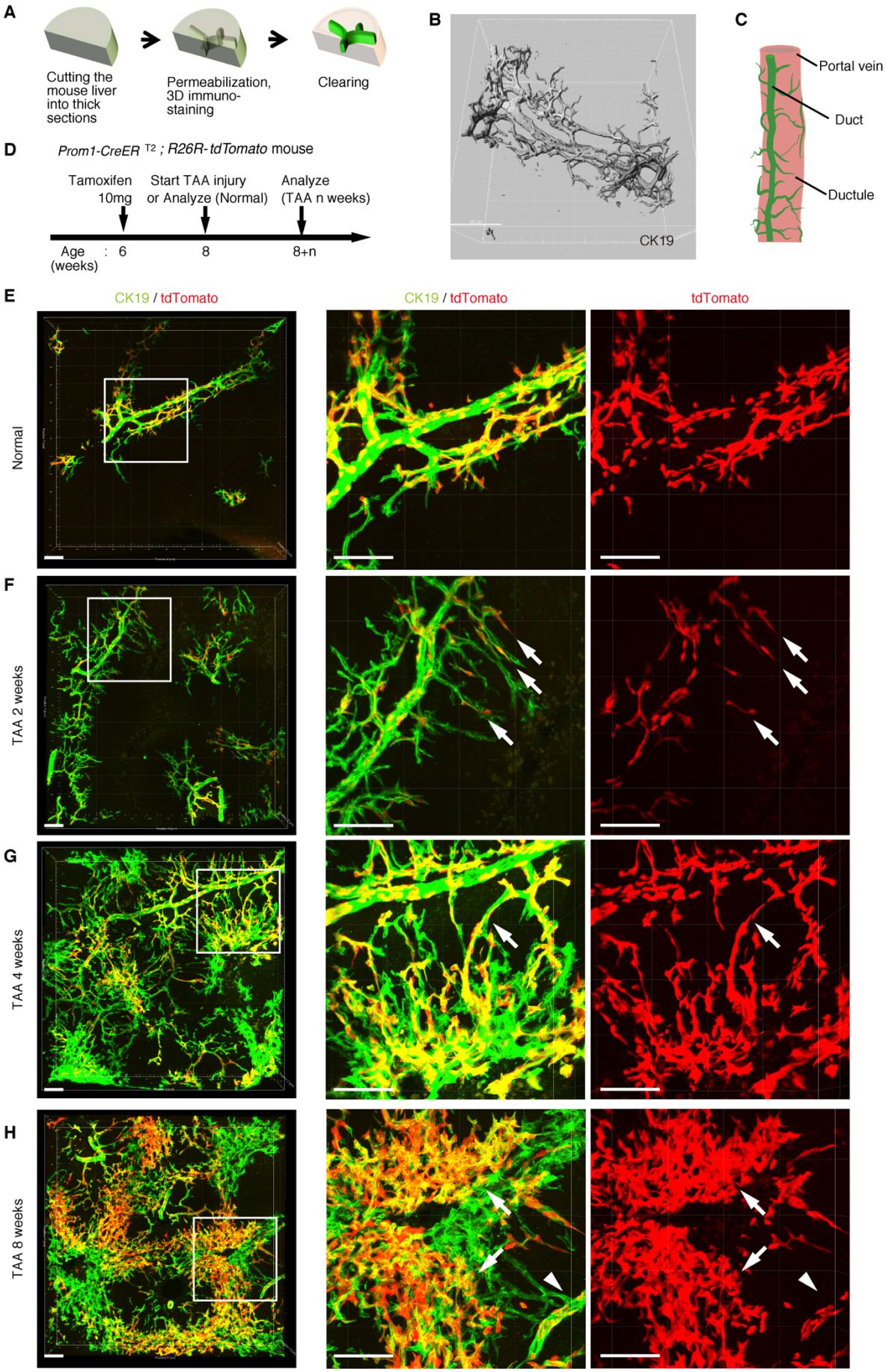
A
Cutting the mouse liver into thick sections
Permeabilization, 3D immuno-staining
Clearing
B
CK19
C
Portal vein
Duct
Ductule
D
Prom1-CreER T2 ; R26R-tdTomato mouse
Tamoxifen 10mg
Start TAA injury or Analyze (Normal)
Analyze (TAA n weeks)
Age (weeks) : 6
8
8+n
E
CK19 / tdTomato
CK19 / tdTomato
tdTomato
Normal
F
TAA 2 weeks
G
TAA 4 weeks
H
TAA 8 weeks

Figure 13. Pre-existing BECs contribute to the nascent biliary epithelial tissue structure upon injury. (**A**) Schematic illustration of the 3D imaging method used to observe biliary tree structures. (**B**) 3D imaging view of the normal biliary tree structure revealed by anti-CK19 immunostaining. Z-stacked images were acquired by confocal microscopy and reconstructed by IMARIS software (normal shading mode). (**C**) Schematic model for the biliary tree structure under the normal condition. (**D**) Experimental scheme. (**E-H**) 3D reconstructed images of the biliary tree revealed by anti-CK19 immunostaining (green), showing the distribution of the BEC lineage-labeled cells (red) in the expanded biliary structure. Serial z-stacked confocal images were tiled (3 x 3 tiles) automatically by automatic positioning stage and Olympus fluoview software. Data are displayed as maximum-intensity projections. A region indicated by a white box in the left panel is magnified in the middle and right panels. Scale bars represent 100 μm. (**F**) White arrows indicate that pre-existing BECs (tdTomato$^+$ cells) are extending outward. (**G**) White arrows indicate a branch of the biliary tree that connects the biliary duct around the PV with newly formed biliary branches around the CV. (**H**) White arrows indicate clusters of labeled cells that are located around the CV. White arrowheads indicate that the duct compartment around the PV shows a uniform mosaic pattern. All experiments were performed with at least five biological replicates.

Pre-existing BECs make a major contribution to the TAA-induced biliary remodeling.

As an experimental model system to study the dynamic morphological changes and cellular behavior of the biliary epithelial tissue, I chose the thioacetamide (TAA)-induced chronic liver injury protocol. TAA is known to induce localized cell death of hepatocytes specifically around the CV. Continuous administration of this drug causes chronic inflammation and bridging fibrosis and eventually leads to tumor formation, reminiscent of the progression of fibrotic and cirrhotic liver disease in human (De Minicis et al., 2013; Yeh et al., 2004). In addition to this pathophysiological relevance, pilot test experiments to compare several injury models also revealed that TAA caused the least auto fluorescence in liver specimens (data not shown), which is suitable and advantageous for obtaining high-quality imaging data to perform analyses on detailed tissue and cellular structures.

Before proceeding with single cell clonal tracing of BECs, I conducted tracing experiments in a condition where BECs were labeled en masse to analyze the pattern of 3D morphological changes of the biliary structure and the relative contribution of the pre-existing BECs to the expanded structures. Beginning 2 weeks after a single administration of the high dose of tamoxifen, the Prom1-CreERT2;R26R-tdTomato mice were continuously administered with TAA (**Figure 13**D). I first confirmed spatial distribution of the labeled cells under normal conditions at the onset of the injury protocol. As shown in **Figure 13**E, the BEC labeling occurred evenly in both the duct and ductule compartments, and in an un-biased mosaic pattern independent of other morphological features such as the duct size or branch locations.

I then analyzed the fate of labeled cells and branching morphogenesis over 8 weeks of the injury (**Figure 13**F-H). The biliary tree structure began to undergo dynamic remodeling by TAA 2 weeks, with ductules, which reside omni-directionally around the PV in normal condition, extending uni-directionally toward the CV. The labeled tdTomato^{+} cells were clearly observed in the extending ductular compartment, indicating that the pre-existing biliary epithelial tissue, presumably the ductule, underwent the morphological changes (**Figure 13**F, white arrows). At TAA 4 weeks, the biliary extension that reached deep into the liver lobule started to form intricately branched structures around the CV area. In these newly formed branches, many tdTomato^{+} cells were

observed. Remarkably, none of the expanded branches lost their connectivity with the main duct in the peri-portal area (**Figure 13**G, white arrows). This indicates that DR is neither the migration of detached BECs or ectopic emergence of BEC-like cells at a distant area in the liver parenchyma, but rather an extension of branching architecture from the pre-existing biliary tissue. Morphological changes further continued along with the disease progression, and at TAA 8 weeks, drastically expanded BECs appeared to make mesh-like network structures (**Figure 13**H).

I observed changes in the distribution pattern of the labeled BECs during the course of the injury progression. While the labeled tdTomato$^+$ cells remained evenly distributed in a mosaic fashion in the main duct structure around the PV (**Figure 13**H, white arrowheads), they displayed apparently uneven distribution in the newly formed structures. That is, the expanded compartment around the CV was composed of several clusters of tdTomato$^+$ cells (**Figure 13**H, white arrows), implicating clonal expansion of a BEC subpopulation therein.

Notably, I found two opposite features, diversity and uniformity, of DR that appeared in micro- and macro- scale observation, respectively. Within each defined region of interest subjected to microscopic observation, the biliary tree exhibited diversity in terms of growth speed and structural features, particularly at its periphery, even in 3D images. Quantitative analysis of BEC distribution in tissue sections supported this notion (**Figure 14**). Taking advantage of the LacZ expression in BECs of the Prom1-CreERT2 mouse strain, I also examined the series of the TAA-induced biliary tissue remodeling by the observation at a totally different macroscopic scale (**Figure 15**). Organ-wide visualization of the entire biliary tree structure enabled me to grasp the landscape of DR, where whole tissue remodeling follows an ordered and uniform pattern with respect to both spatial and temporal changes.

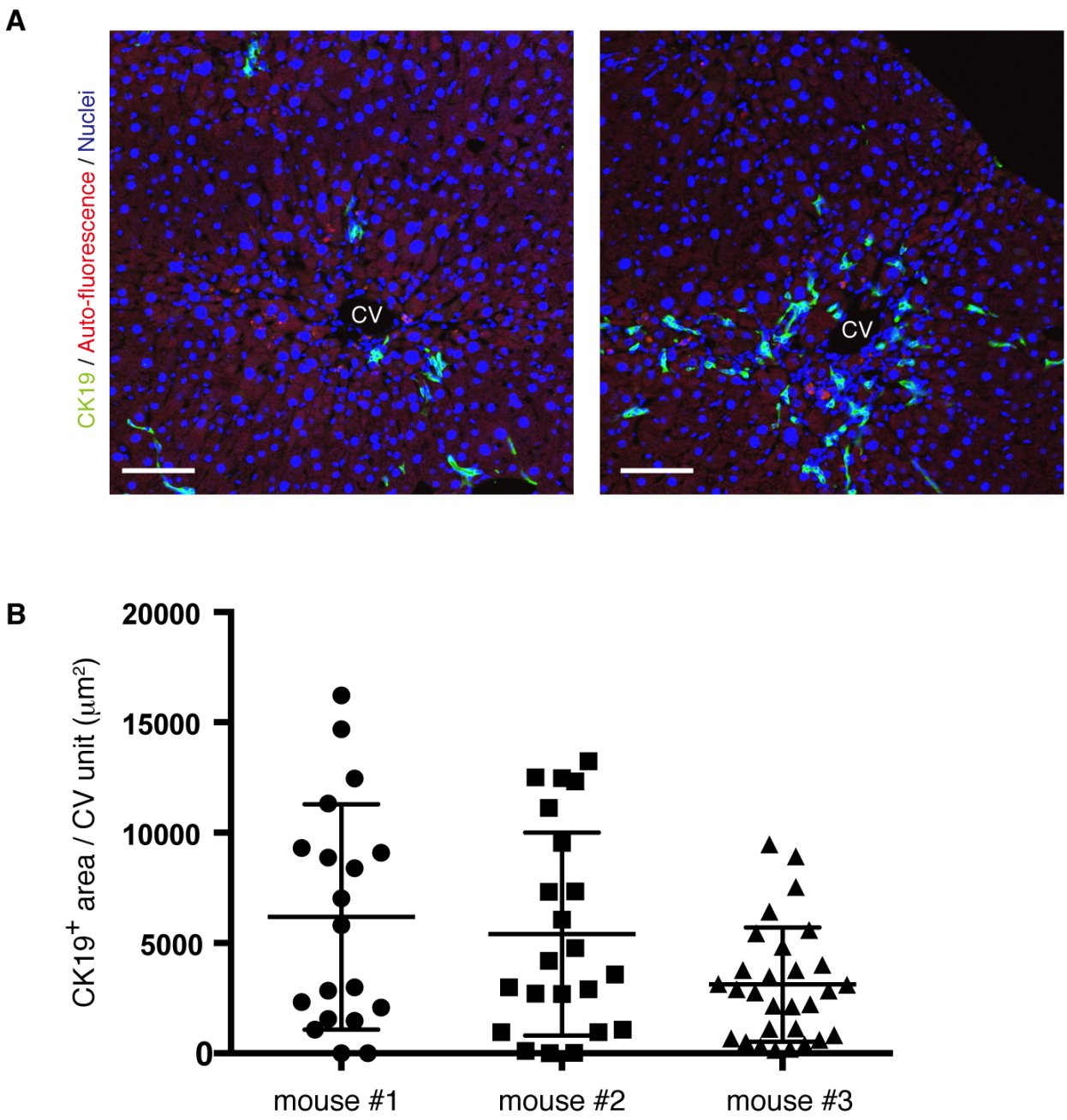

Figure 14. The level and distribution pattern of the DR in a microscopic view is highly diversified within a liver. (**A**) Progression of the DR is not uniform microscopically. Sections were prepared from different regions of the same liver sample derived from a mouse treated with TAA for 6 weeks, and then immunostained with anti-CK19 antibody to reveal the biliary tree structure. Note that the level and distribution pattern of the DR appear considerably diversified even in the same liver when I focus on relatively small areas. (**B**) The area of $CK19^+$ regions in different CV units (>18 per mouse) was quantified by using Volocity software and plotted to show highly divergent levels of

biliary tree expansion in each liver. Three different mice treated with TAA for 6 weeks were analyzed.

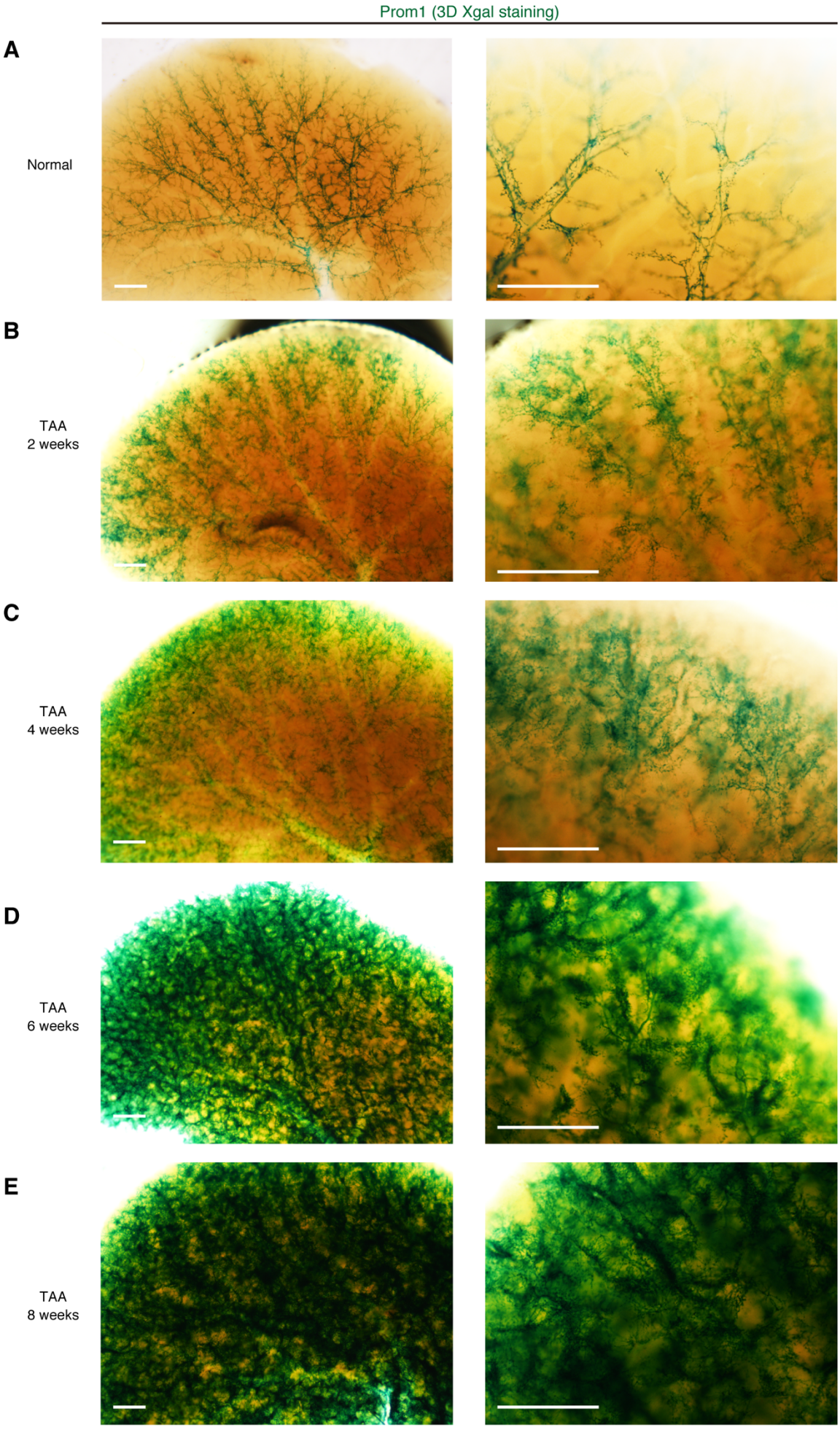
Prom1 (3D Xgal staining)
A
Normal
B
TAA
2 weeks
C
TAA
4 weeks
D
TAA
6 weeks
E
TAA
8 weeks

Figure 15. Macroscopic view of the DR upon TAA injury over time. The entire structure of the biliary tree was visualized by whole-mount X-gal staining of the liver from the Prom1-CreERT2 mice harboring the nLacZ gene knocked-in to the Prom1 locus. Whole-liver samples were harvested, fixed, stained and cleared with clearing reagent. Images were acquired with a macro zoom microscope (Olympus MVX10). Green signals represent nuclei of the $Prom1^{+}$ cells. Scale bars, 1 mm. (**A**) $Prom1^{+}$ signals revealed the finely branching biliary tree structure under the normal condition. The duct and ductule units can be clearly recognized, delineating the PV. (**B** and **C**) Upon TAA-induced injury, fine branches of the biliary tree extend from around the PV outward to the liver parenchyma. (**D** and **E**) After extensive branching and proliferation, BECs ($Prom1^{+}$ cells) occupied the entire liver lobule. Note that the DR proceeds in a relatively stereotyped manner throughout the liver.

The results of the BEC lineage tracing in the 3D tissue architecture strongly suggested that the pre-existing BECs made a major contribution to DR in the TAA injury model, at least within the initial period of 8 weeks. It should be noted that, in the present experimental setting, virtually all of the labeled cells were contained within the $CK19^+$ cell population while labeled hepatocytes were rarely detected (**Figure 13**H). This result is consistent with recent reports by many other groups based on lineage tracing experiments, in that the cells induced and expanded by DR, or LPCs, do not show stem/progenitor cell-like activity to contribute to new hepatocytes in most, if not all, mouse liver injury models (Grompe, 2014; Tarlow et al., 2014a; Yanger et al., 2014).

Hepatocytes are not the main source of newly formed BECs

Based on the above results of the 3D tracing of BECs, I assumed that pre-existing BECs were the main source of the newly formed biliary structure. However, several studies recently reported that hepatocytes are capable of converting into BEC-like cells upon liver injury (Nagahama et al., 2014; Sekiya and Suzuki, 2012; Tanimizu et al., 2014; Tarlow et al., 2014a). I thus sought to employ a complimentary lineage tracing strategy to directly evaluate the contribution of hepatocytes as an alternative source of the expanded biliary structure upon TAA-induced DR.

AAV-mediated hepatocyte labeling and lineage tracing

For lineage tracing of hepatocytes, I used a recombinant adeno-associated virus vector pseudo serotype with capsid 8 (rAAV2/8) expressing an improved version of the Cre recombinase (iCre) gene. The rAAV2/8 vector is well known to target hepatocytes in mouse livers in a highly specific and efficient manner, and has been used in many studies for gene transfer into hepatocytes in vivo. Importantly, it does not transduce BECs in the adult mouse livers (Yanger et al., 2014). I injected rAAV2/8-iCre into the R26R-tdTomato mice to permanently label hepatocytes (**Figure 16**). FACS analysis of liver cells isolated from these mice confirmed that almost all hepatocytes were labeled (more than 97 %; **Figure 16**B), while $EpCAM^+$ BECs were not labeled (less than 0.1 %; **Figure 17**B). I prepared genomic DNA from sorted cells, and analyzed the DNA recombination in the tdTomato-positive cells and -negative cells (**Figure 18**). The fluorescent pattern was completely matched with the DNA recombination patterns, indicating that the experimental system was worked accurately. I

also confirmed the specificity and efficiency of the rAAV2/8-iCre mediated labeling by using immunohistological analysis (**Figure 16**C).

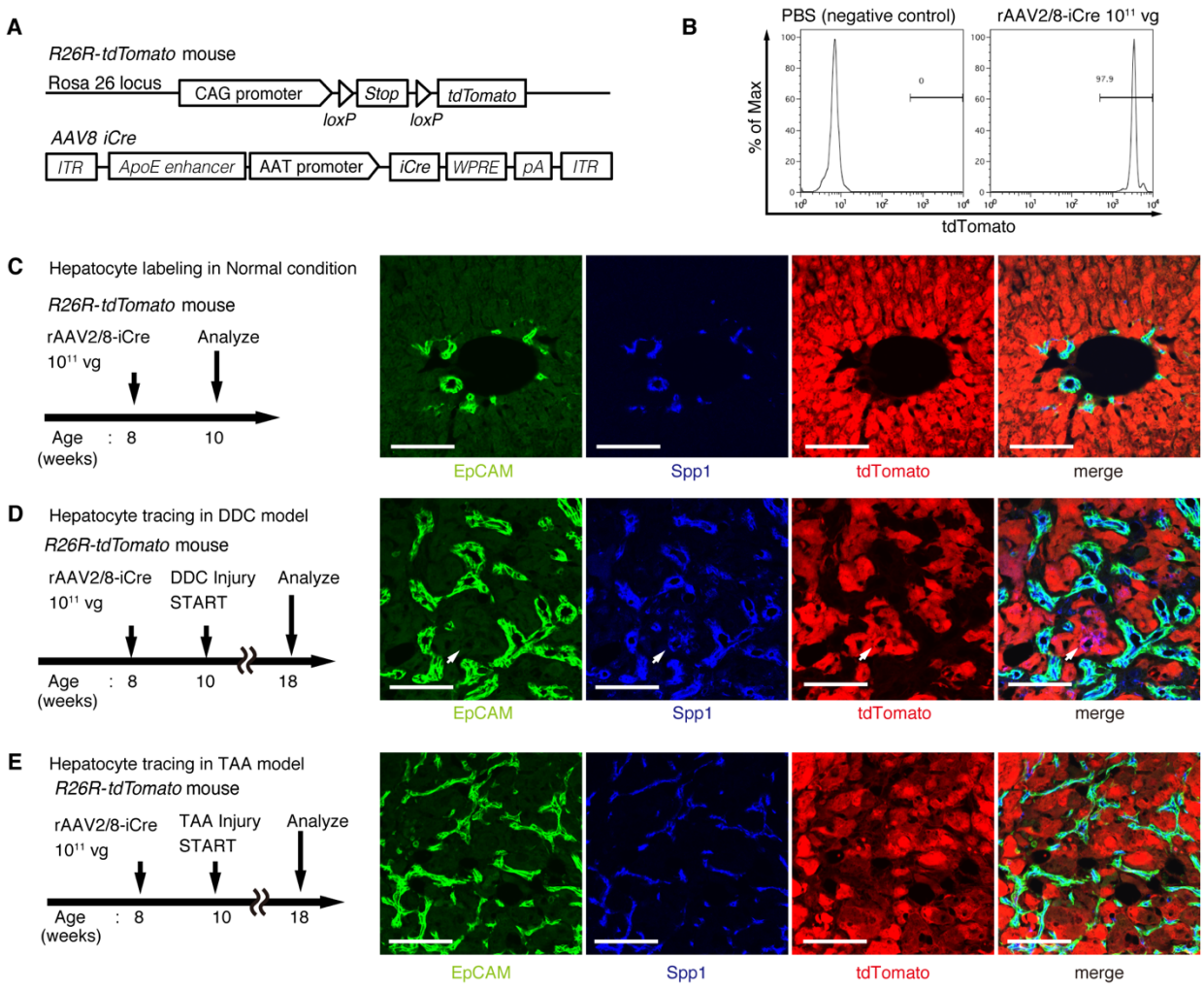

Figure 16. Immunostainig experiments for lineage tracing of hepatocytes. (**A**) R26R-tdTomato mice were used in combination with rAAV2/8-iCre for the labeling of hepatocytes. rAAV2/8-iCre is designed to transduce only hepatocytes. (**B**) Representative image of FACS analysis of hepatocytes labeled by rAAV2/8-iCre. These histogram images show the result of serial purification gates (FSC/SSC, pulse width, $DAPI^-$). (**C**) Adult R26R-tdTomato mice were injected with rAAV2/8-iCre ($1x10^{11}$ vg /mouse). 2 weeks after injection, the mice were sacrificed and the livers were stained with anti-EpCAM and anti-Spp1 antibody (scale bar, 100 um). (**D** and **E**) Mice were injected with rAAV2/8-iCre (10^{11} vg /mouse) and then subjected to a 3,5-diethoxycarbonyl-1,4-dihydrocollidine (DDC) or TAA injury model. $tdTomato^+$ $Spp1^+$ $EpCAM^-$ cells were only observed in DDC-fed mouse liver sections (white arrows). Analysis was done with 5 mice per each injury model. More than 6 sections were made per mouse.

Here, lineage tracing experiments of hepatocytes were performed in the TAA injury model as well as in the DDC injury model, as the latter was used in recent reports to convincingly demonstrate the contribution of hepatocytes to the proliferating duct cells (Tanimizu et al., 2014; Tarlow et al., 2014a). I analyzed expression of several molecular markers related to BECs including EpCAM, CK19, Prom1, Spp1, and MIC1-1C3. Upon DDC administration for 8 weeks, I detected many $Spp1^+$ cells in the tdTomato-labeled population, but did not detect any $EpCAM^+$ $tdTomato^+$ cells (**Figure 16**D). This indicates that while hepatocytes can indeed gain a "biliary" phenotype in terms of Spp1 expression, they are still not fully converted to BECs as defined by EpCAM expression. FACS analysis using the MIC1-1C3 surface antigen instead of Spp1 also revealed that hepatocytes contributed to the $MIC1\text{-}1C3^+$ "biliary" population but not to that of the EpCAM subset (**Figure 17**C). I also examined the expression patterns of Prom1 and CK19 and found that they were essentially the same as that of EpCAM but were different from those of Spp1 and MIC1-1C3. These results are consistent with the previous report by Tarlow et al., (Tarlow et al., 2014a)(**Figure 20**, **Figure 21**) , showing that $Spp1^+$ $MIC1\text{-}1C3^+$ proliferating ductular cells that derived from hepatocytes upon DDC injury (which named as hepPDs) are phenotypically distinct from those derived from pre-existing BECs (which they named as bilPDs) with respect to the gene expression profile. Specifically, such hepatocyte-derived cells (hepPDs) show little or no expression of CK19, EpCAM, or Prom1.

I also estimated the contribution of hepPDs to the biliary population using this BEC labeling system, where a decrease in labeling ratio of BECs could be expected if a large number of hepatocytes converted into BECs. I found no significant decrease of labeling ratio after DDC administration in EpCAM cells. The ratio might be slightly decreased in MIC1-1C3 cells, which remained to be confirmed as statistically significant (**Figure 19**). Considering the relatively small contribution of the hepatocyte-derived cells to the entire MIC1-1C3 population upon DDC injury (1.88% in **Figure 17**C), the result is overall consistent with that of the hepatocyte tracing experiments using the AAV system.

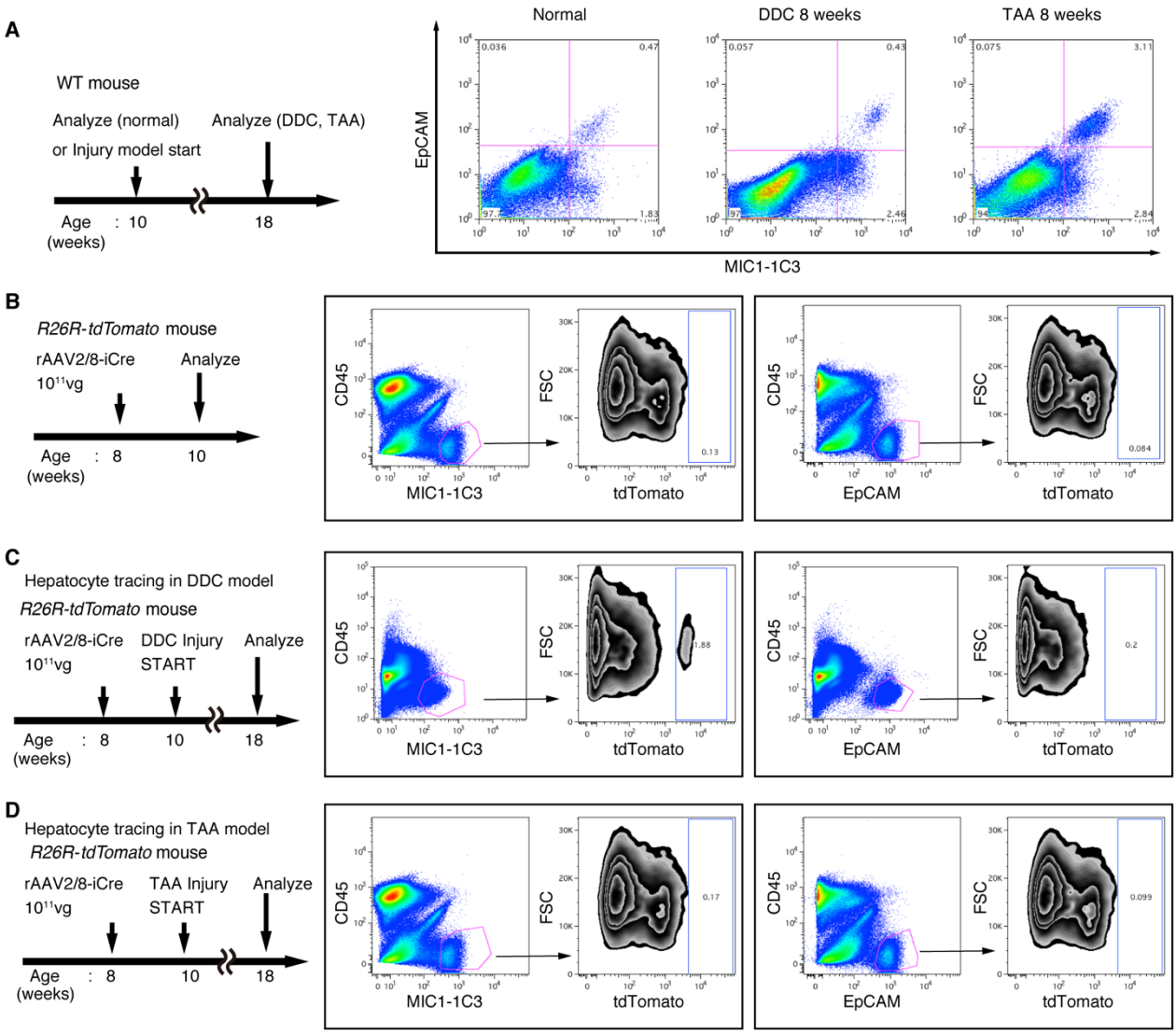

Figure 17. FACS analysis for lineage tracing of hepatocytes. The experimental design is described on the left side of the figure. Hepatocytes of R26R-tdTomato mice were labeled with rAAV2/8-iCre. Dissociated liver cells were stained with anti-MIC1-1C3 antibody, anti-EpCAM antibody, anti-CD45 antibody and anti-Prom1 antibody. The results for Prom1 are not shown because they were essentially the same as those for EpCAM. All experiments were done more than three times to confirm reproducibility. Sequential FACS gates were applied; $DAPI^-$ (live cells), FSC/SSC, and pulse width. (**A**) All $EpCAM^+$ cells were included in the $MIC1\text{-}1C3^+$ cell population. (**B**) Before injury, almost no $MIC1\text{-}1C3^+$ or $EpCAM^+$ cells were labeled. (**C**) After DDC injury, a $tdTomato^+$ population emerged in the $MIC1\text{-}1C3^+$ population. Meanwhile almost no labeled cells emerged in the $EpCAM^+$ population. (**D**) After TAA injury, almost no $tdTomato^+$ cells appeared in $MIC1\text{-}1C3^+$ population or in the $EpCAM^+$ population. Experiments were performed with three biological replicates and representative results are shown.

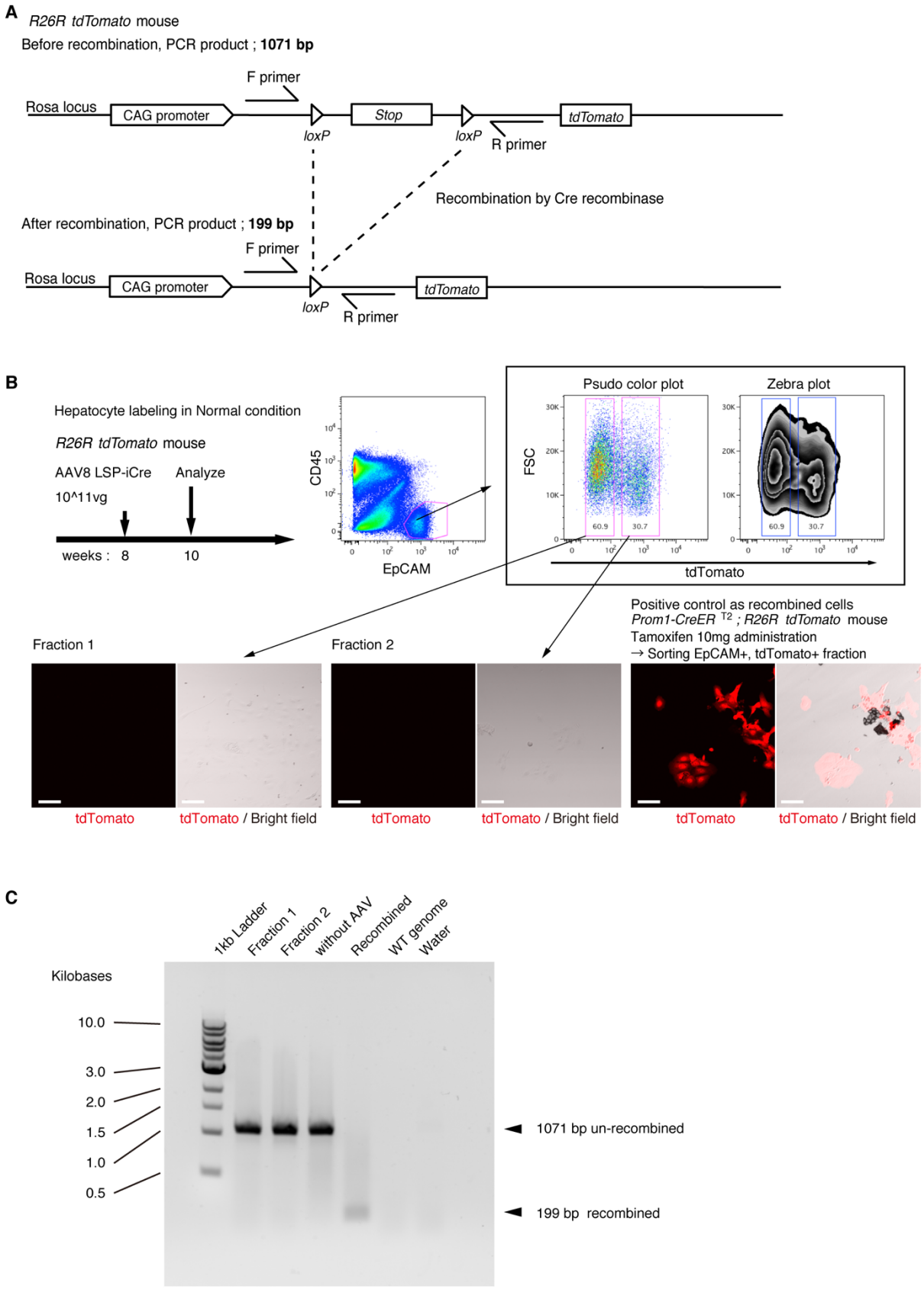

Figure 18. Validation of DNA recombination in the Cre-loxp system (**A**) Illustration of DNA recombination by the Cre-loxp system. R26R-tdTomato mice were used to label cells with fluorescent protein. iCre expressed by AAV recombines DNA, shortening genomic DNA by ~800 bps.

(**B**) FACS analysis was performed to detect and collect tdTomato$^+$ cells in EpCAM$^+$ cells. Without liver injury, EpCAM$^+$ cells were classified into two fractions, and sorted. In both fractions, fluorescence of tdTomato was not detected. As a positive control for recombined cells, tdTomato$^+$ cells from Prom1-CreERT2;R26R-tdtomato mice were used here. (**C**) DNA recombination was evaluated by PCR of genomic DNA. Unexpected DNA recombination of genome DNA of BECs was not detected, while recombination of positive control DNA was correctly detected.

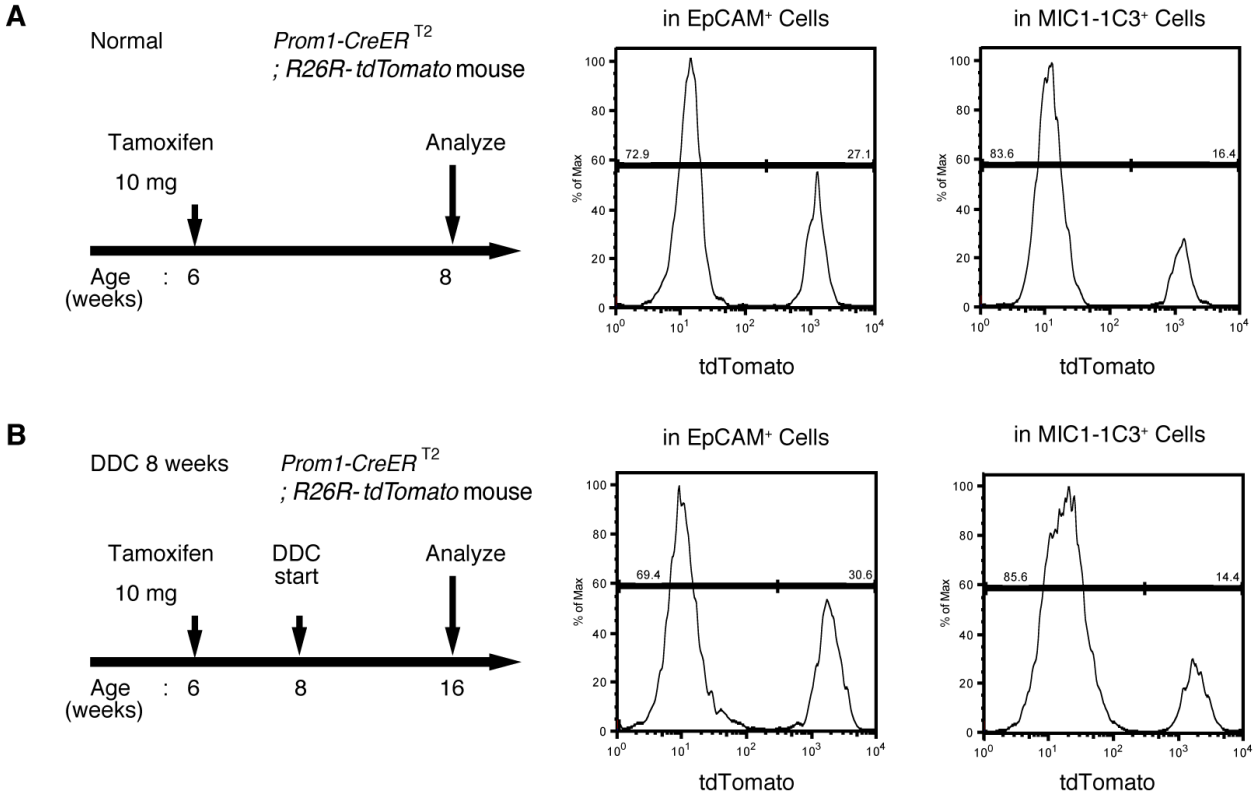

Figure 19. Quantification of labeling ratio in the Prom1-CreERT2;R26R-tdTomato mice before/after DDC injury. (**A** and **B**) Labeling ratio in EpCAM$^+$ or MIC1-1C3$^+$ cell populations in the Prom1-CreERT2;R26R-tdTomato mice was evaluated by FACS. The left panels show the experimental design. Non-parenchymal cells were collected from the dissociated liver and stained with anti-EpCAM antibody or anti-MIC1-1C3 antibody. FACS gates were applied sequentially as follows: DAPI$^-$ (live cells), FSC/SSC, pulse width, CD45$^-$, and EpCAM$^+$ or MIC1-1C3$^+$.

In the TAA model, I did not detect the emergence of hepatocyte-derived EpCAM$^+$ cells, similar to the results of DDC model (**Figure 16**E). Intriguingly, even hepatocyte-derived Spp1$^+$ cells were not detected, suggesting that hepPDs are not induced under the injury condition of TAA model. Consistently, FACS analysis detected no MIC1-1C3$^+$ cells or EpCAM$^+$ cells in the tdTomato$^+$ population (**Figure 17**D), further confirming the notion that hepatocytes do not convert into either BECs (or bilPDs) or BEC-like cells (or hepPDs) in the course of TAA-induced liver injury even after 8 weeks. Thus, Spp1 and MIC1-1C3 mark a different and broader cell population compared with the one defined by the expression of CK19, EpCAM and Prom1. I concluded that hepatocyte-derived duct-like cells (hepPDs) do emerge in the DDC model but not in the TAA model, and that they are distinguishable from bilPDs (**Figure 21**). This finding may be of pathophysiological relevance, in that the DDC model represents as a cholestatic liver injury model that primarily targets the biliary epithelial system, while TAA as a hepatotoxic injury model with less severe cholestatic disease phenotypes.

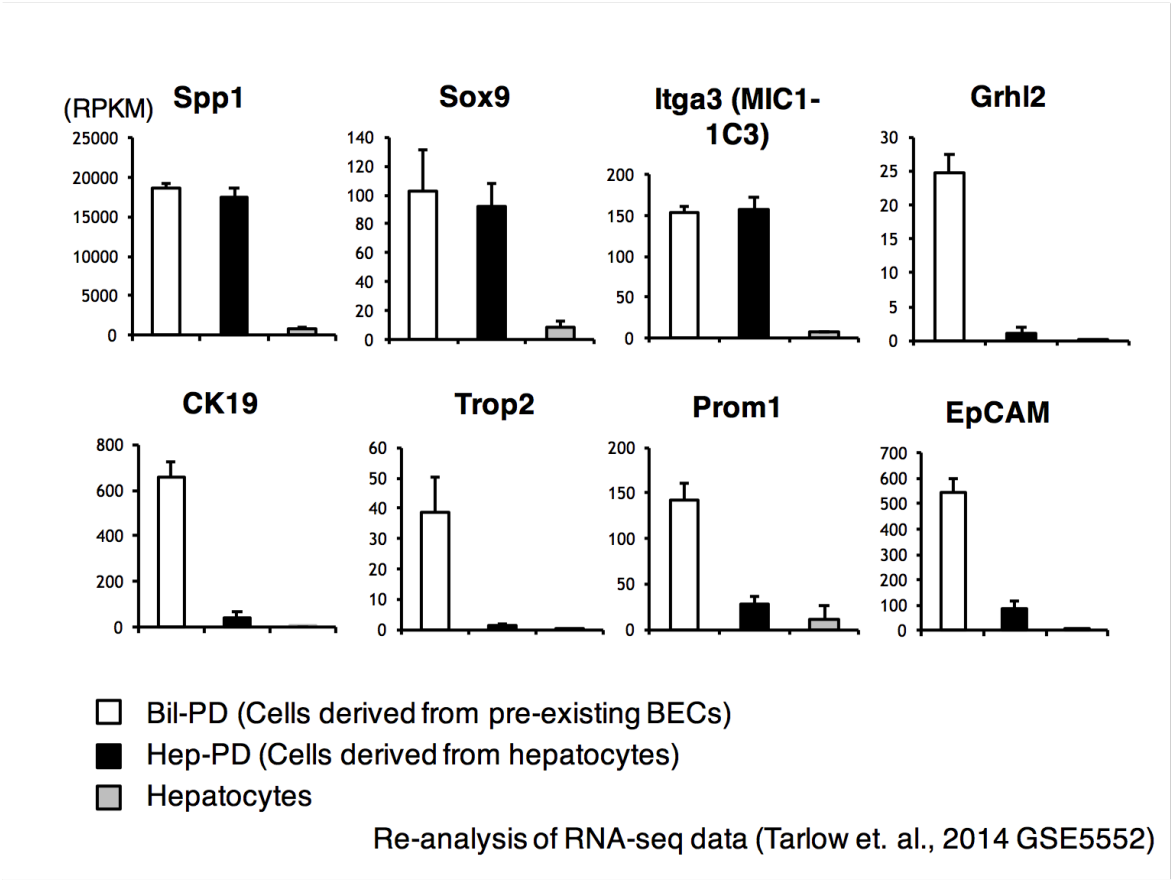

Figure 20. Re-analysis of various BEC marker genes in RNA-seq data published in the of previous study. RNA-seq data (GSE5552) was downloaded from Gene Expression Omnibus (GEO). Biliary epithelial marker genes were shown as bar graph (error bars indicate SEM).

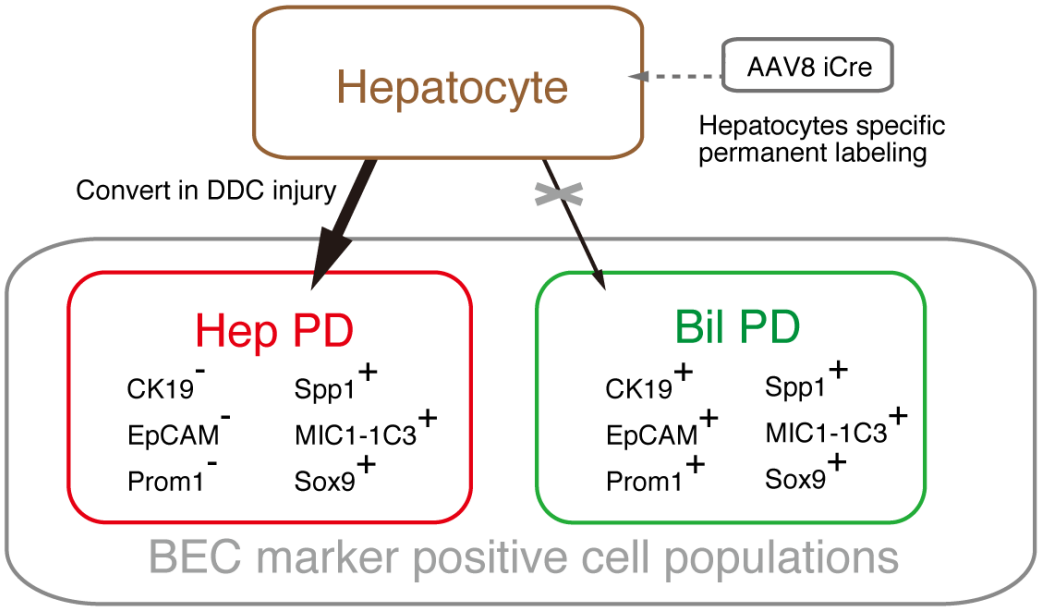

Figure 21. Schematic illustration of lineage conversion between BECs and hepatocytes

3D structures of hepPDs and bilPDs

To gain an insight into the spatial relationship between hepPDs ($Spp1^+$ $EpCAM^-$ cells) and the biliary tissue structure composed of bilPDs ($Spp1^+$ $EpCAM^+$ cells), I further applied the 3D immunostaining and imaging analyses. 3D images confirmed that hepPDs were barely detected under physiological condition or upon TAA-induced injury. In the DDC model, however, hepPDs emerged around several parts of the pre-existing biliary architecture (**Figure 22**). The tissue architecture composed of hepPDs was different from the one composed of bilPDs; the former did not exhibit any single and contiguous branch structure but rather formed a subsidiary structure located just around the pre-existing branched structures of the latter.

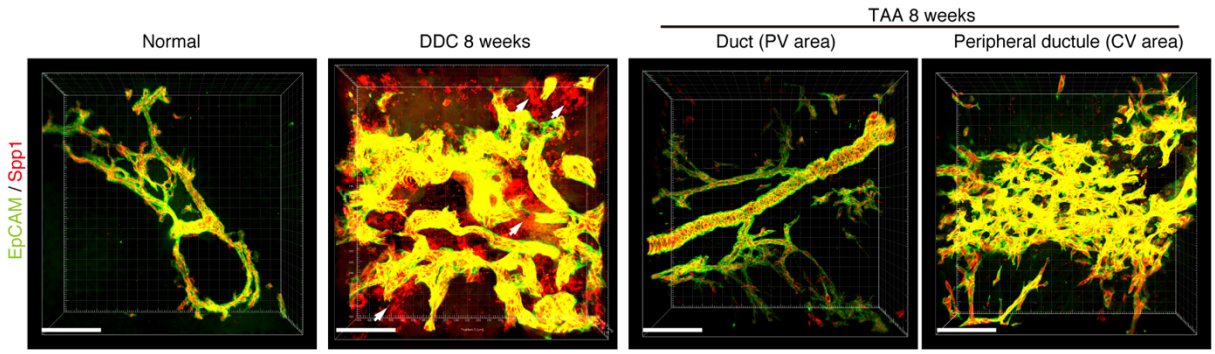

Figure 22. 3D imaging of the biliary tree in various conditions. 3D imaging was performed with WT mice (normal state, DDC for 8 weeks, TAA for 8 weeks). Acquired z-stack data are displayed as the maximum-intensity projection after contrast adjustment with IMARIS software. In the DDC liver, $Spp1^{+}$ $EpCAM^{-}$ cells were observed (white arrow) around main biliary tubular structures that were composed of $EpCAM^{+}$ cells.

These results of fate tracing and 3D-imaging analyses revealed that, while hepatocytes were capable of being converted into the biliary epithelial state in a context-dependent manner, the main contributor to DR was pre-existing BECs in terms of gene expression, cell number, and 3D structure. Thus, I have focused the fate and behavior of the pre-existing BECs to understand the cellular basis of DR, particularly when using the TAA model. I have to note that this study does not refute the existence of hepatocyte-to-biliary phenotypic conversion, nor its contribution to liver regeneration. I wish to point out that hepPDs and bilPDs are different and they should be discussed separately (**Figure 21**).

BECs exhibit widespread heterogeneity in proliferative capacity in situ.

Based upon the notion that the nascent biliary structure is formed upon TAA injury through the biliary epithelial tissue-intrinsic cell growth, I set out to perform quantitative single BEC tracing experiments in vivo using this model to elucidate the cellular basis of this dynamic tissue remodeling process (**Figure 23**A, B). The Prom1-CreERT2;R26R-tdTomato mice were administered with a very low dosage of tamoxifen to label BECs at a very low frequency. 3D imaging and FACS analyses showed that the labeling was introduced at a rate of less than 0.2 % of total BECs and that the labeled cells located singly and apart from each other (**Figure 23**C, D). After single cell labeling, mice were subjected to the TAA protocol and the size of single cell-derived clonal progenies was analyzed during the course of injury progression. Of note, the labeling index of 0.2 % did not change even after the injury period, which is consistent with the notion that the labeling was introduced in an unbiased manner under this low frequency labeling condition (**Figure 24**). After 6 weeks of injury, there were still many BECs that had rarely divided and remained single or merely as clusters composed of a few cells. At the same time, I also observed larger colonies composed of dozens of cells, indicating that some BECs had undergone several rounds of cell division (**Figure 23**E, F). This clearly indicates that the BEC population does not proliferate uniformly as a whole upon injury, but rather, exhibits heterogeneity with regard to their proliferative capacity in vivo.

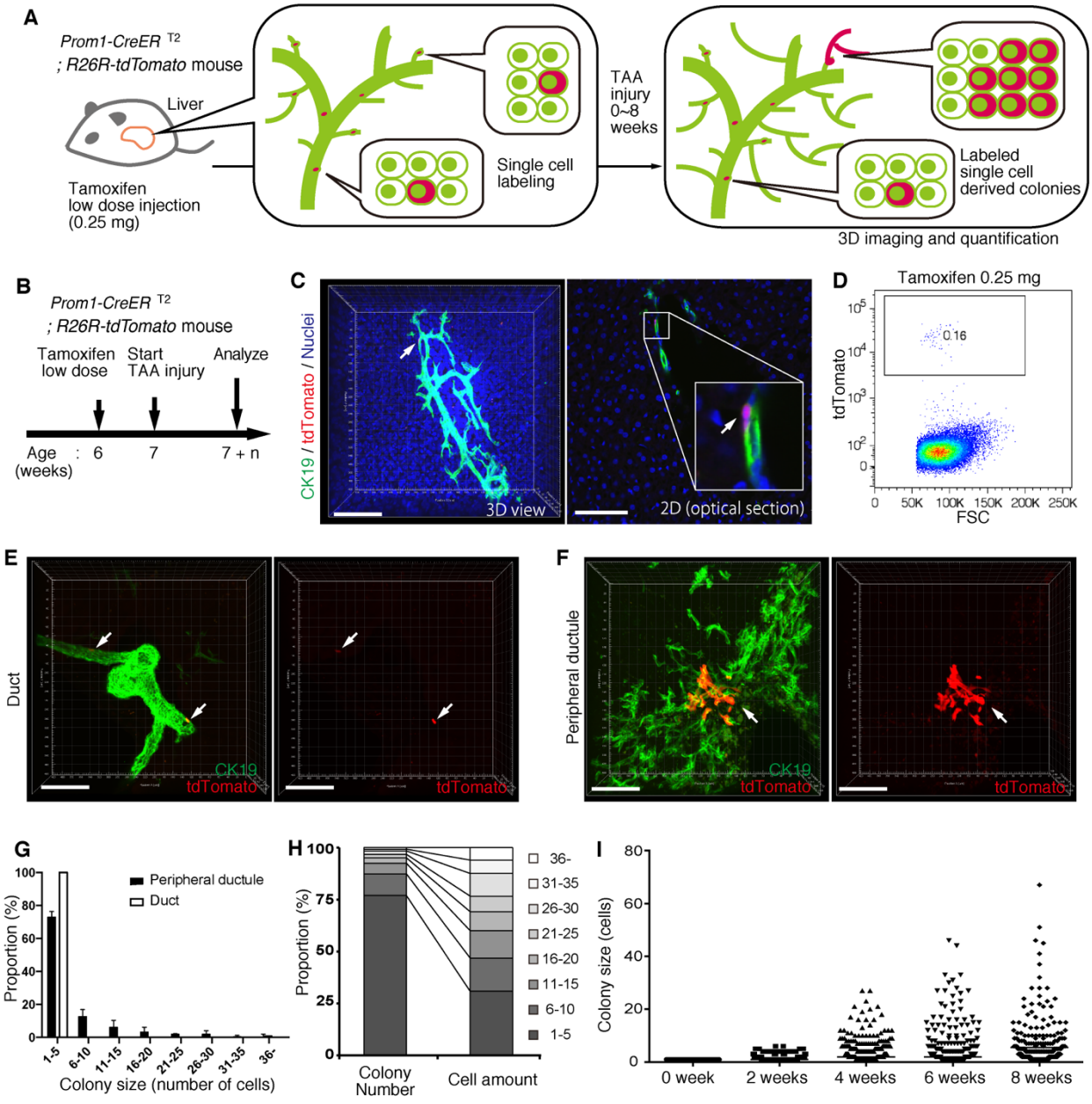

Figure 23. BECs exhibit heterogeneity in terms of proliferative capacity in vivo. (**A**) Schematic diagram showing the rationale for quantitative in vivo single-BEC tracing. (**B**) Experimental design. (**C**) Upon administration of a very low dosage of tamoxifen (0.25 mg/kg body weight), liver samples were stained with anti-CK19 antibody and Hoechst33342. BEC labeling was introduced at the single-cell level (white arrows). A 3D image and an optical section corresponding to the same visual field are shown in the left and right panels, respectively (scale bars, 100 mm). (**D**) Quantification of the BEC- labeling efficiency after the low-dosage tamoxifen injection. For FACS analysis, successive gates were applied for $DAPI^-$, FSC/SSC, pulse width and $EpCAM^+$ (not shown). A representative plot pattern for 4 biological replicates is shown. (**E** and **F**) 3D images of labeled

colonies after 6 weeks of TAA injury. Thick sections were stained with anti-CK19 antibody and 3D images were acquired with tdTomato^{+} colonies (white arrows) using confocal microscopy. The data are shown as maximum intensity projections. (**E**) Duct compartment around the PV area. (**F**) Peripheral ductule compartment around the CV area (scale bars, 100 μm). (**G**) Distribution of the quantified colony size at TAA 6 weeks (n = 5 mice, mean ± SD). The colonies were classified into two categories (duct and peripheral ductule) as described in the 'Materials and methods' section. (**H**) Relative numbers of colonies categorized by colony size as depicted in the legend to the right (left stacked bar chart), and the relative contribution of cell numbers from each colony category (right stacked bar chart) (calculated as follows: 100 x (sum of the cell numbers in a colony size)/ (sum of all the counted cell numbers)). (**I**) Scatter plot of the colony size distribution over time. Data from five mice were pooled for each time point (total colony numbers counted were 257, 272, 304, 307 and 310 for the 0, 2, 4, 6 and 8 week samples, respectively). Horizontal lines show the mean of colony size. Images shown in panels (**C**), (**E**), and (**F**) are representative data for at least 5 biological replicates.

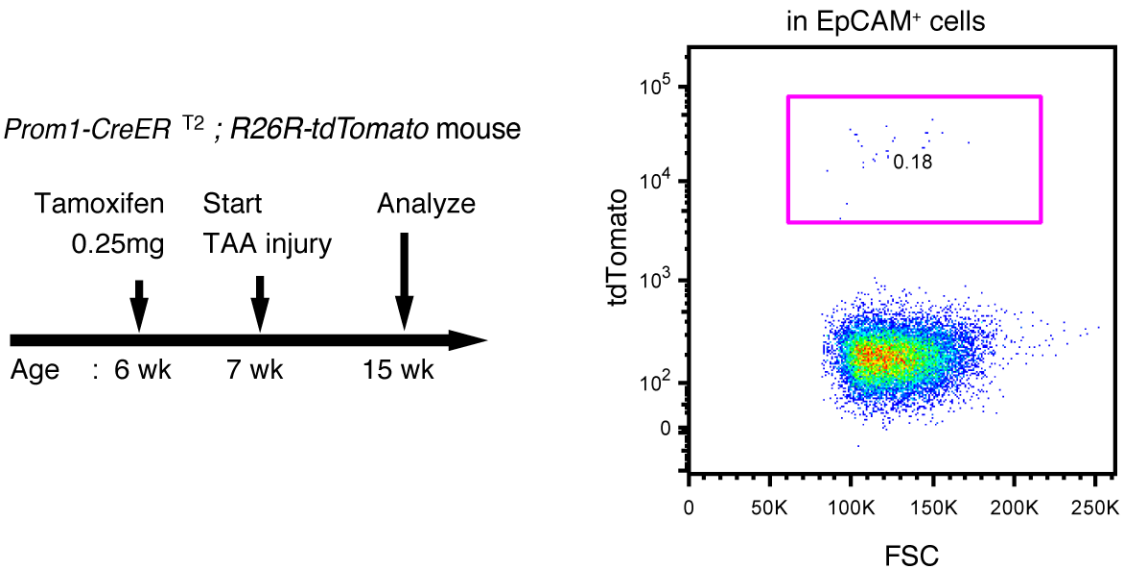

Figure 24. Labeling ratio in the Prom1-CreERT2; R26R-tdTomato mice was not changed after 8 weeks of TAA injury. The left panel shows the experimental design. Mice were subjected to TAA injury after the low-dosage tamoxifen injection (0.25 mg/kg body weight). Before injury, the labeling ratio of BECs was less than 0.2 % (around 0.18 %). Changes of labeling ratio were quantified after TAA injury. For FACS analysis, successive gates were applied for $DAPI^-$, FSC/SSC, pulse width and $EpCAM^+$ (not shown). Experiments were performed with 3 biological replicates and representative results are shown.

Taking advantage of the 3D imaging, I quantified the exact size (i.e., the numbers of constituting cells) of each single cell-derived clone in the liver tissue. On quantification, I classified the biliary epithelial tissue into two distinct portions according to tube diameter sizes and locations, namely "duct" and "peripheral ductule", as I anticipated a putative relationship between the tissue architecture and cell proliferation capacity. This led me to find two important features about the colony size distribution. Firstly, the duct compartment did not contain any large colony that consisted of more than five cells, while the peripheral ductule compartment did (**Figure 23**E-G). Notably, I did not find any large colony that was directly connected to the duct cells adjacent to PV. It is thus not likely the case that some proliferative cells reside in a fixed position in the duct compartment, akin to the intestinal stem cells locating in the crypt bottom, and continuously supply progeny toward the periphery. Rather, the colony-initiating, proliferative cells may reside in the peripheral ductule compartment and relocate their position upon parenchymal injury.

The second feature is the pattern of colony size distribution. I initially assumed it to be a bimodal shape, with one peak corresponding to a non-proliferative population and the other to a proliferative one. However, the data rather showed a unimodal distribution pattern with long tail (**Figure 23**G and I). Although the proportion of the number of the large colonies was seemingly low, they actually accounted for a large proportion among the total proliferated cells by considering the numbers of cells in each colony (**Figure 23**H). The results thus highlight a proliferative and expandable subpopulation of BECs that should make a major contribution to the biliary epithelial tissue growth.

Proliferating BECs are not strictly compartmentalized in a specific tissue structure.

I further sought to reveal the relationship between cell proliferation and tissue structure in detail. In many tissues, proliferating cells, or stem cells, are spatially arranged within a specific area with a characteristic tissue structure, such as the case with intestinal stem cells residing in the crypt bottom of the intestinal epithelium (Barker et al., 2007). I searched the biliary tree in 3D for any structural feature corresponding to the location of cycling cells by immunostaining for the cell proliferation marker Ki67.

Most of the Ki67$^+$ BECs localized to the peripheral area of the biliary tree in the TAA injured liver, while only a few Ki67$^+$ BECs were observed in the duct around the PV area (**Figure 25**). This distribution pattern fits well with the results of the clonal cell tracing data. In the peripheral ductule compartment, the Ki67$^+$ cells were widely scattered. No further sign of defined stem cell niche, such as a cluster or aligned arrangement of Ki67$^+$ cells, was observed.

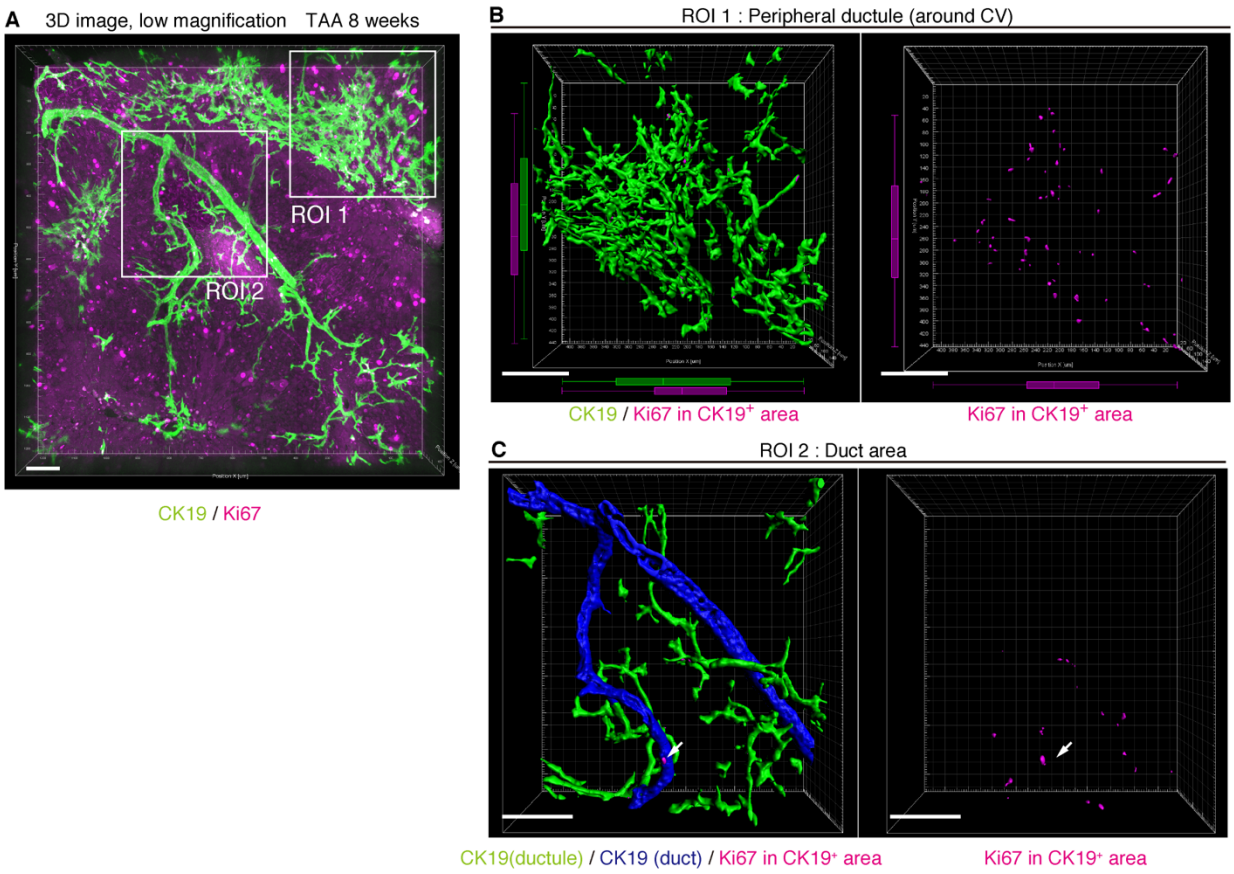

Figure 25. 3D visualization of Proliferating BECs at TAA 8 weeks. (**A**) 3D images of the biliary tree (CK19 immunostaining; green) and the cell cycle marker Ki67 (magenta) in TAA-injured liver samples. (**B**) Magnified views of the region of interest (ROI) 1 were shown. In right panel, $CK19^+$ area and $Ki67^+$ BECs therein were extracted using the IMARIS surface protocol. Distribution patterns of the $CK19^+$ area and the $Ki67^+$ $CK19^+$ cells were calculated using the IMARIS vantage protocol after the signals were projected onto the background, and depicted in 2D box-and-whisker plots. (**C**) 3D images corresponding to the ROI 2 area represent the duct compartment of a mouse liver at TAA 8 weeks. Signals of 3D immunofluorescence for CK19 and Ki67 (magenta) were converted into 3D graphics using the surface protocol of the IMARIS software. The duct and ductule compartments are colored in blue and green in the left panel, respectively. Only one $Ki67^+$ nuclei was found in the duct compartment, whereas there are many in the ductules.

At 2 weeks of TAA administration, $Ki67^{+}$ BECs were already enriched in the peripheral ductule region rather than the ducts and scattered therein (**Figure 26**), suggesting that the mode of proliferation is maintained over time.

I also examined the distribution pattern of proliferating BECs by continuous labeling of cycling cells using 5-bromo-2'-deoxyuridine (BrdU) incorporation, and obtained the same result (**Figure 27**).

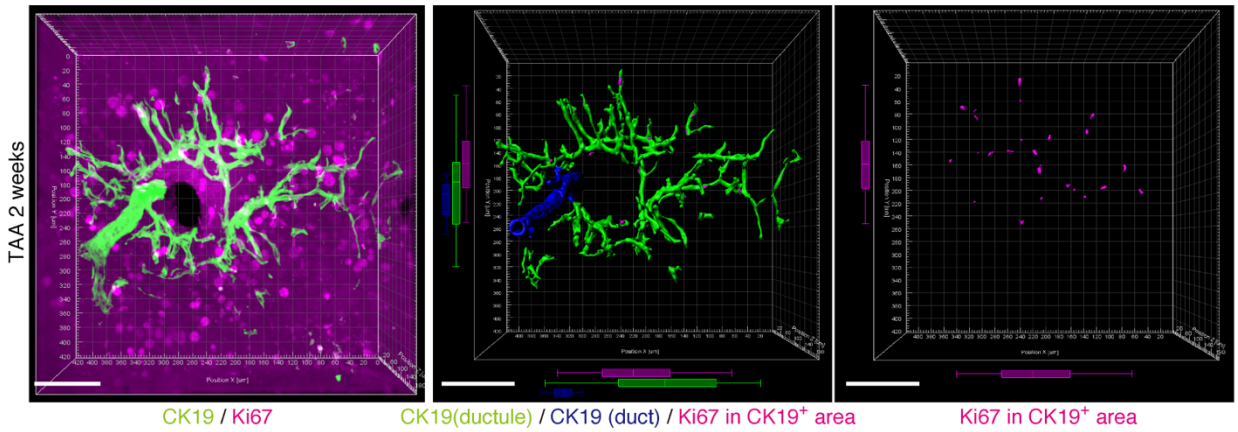

Figure 26. 3D visualization of Proliferating BECs at TAA 2 weeks. Liver samples at TAA 2 weeks were visualized in 3D images. Biliary structure is classified into duct compartment (shown in blue in the center image) and ductule (green).

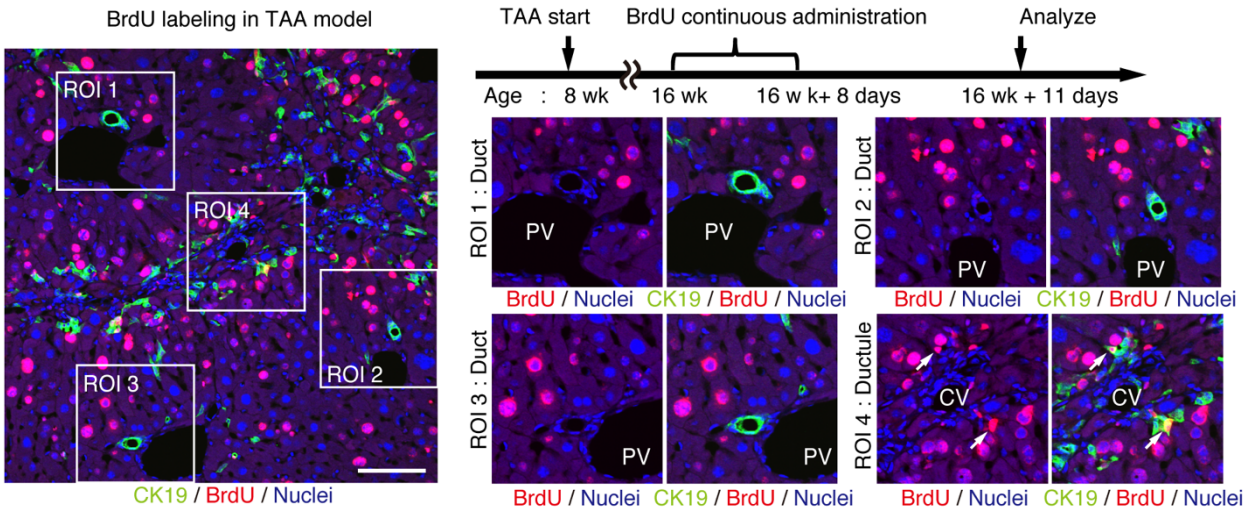

Figure 27. BrdU continuous uptake experiments. Proliferating cells were labeled by continuous administration of BrdU for 8 days in the course of the TAA injury and were analyzed by anti-BrdU immunostaining (magenta). BrdU incorporation was observed in BECs residing in the peripheral ductule compartment (white arrows), but rarely in those in the duct compartment.

BECs can take two different states in the modes of proliferation.

From the quantitative single cell tracing data, I revealed the heterogeneity among BECs with regard to their proliferative capacity in vivo. To understand the mechanistic basis for such heterogeneity, I sought to construct a simple growth model that could potentially explain and be used to simulate the proliferative behavior of BECs upon injury. For this purpose, it was necessary to collect information about cellular events in a short time scale. I hypothesized that BECs could be classified into two states based on their temporal proliferative capacities, and if this is the case, the relationship between these states should then be examined.

I designed an experiment to investigate the temporal proliferative state and cell fates of BECs using two nucleotide analogs, BrdU and EdU, as has been employed in a previous study on pancreatic progenitor cells (Teta et al., 2007). First, mice were administered with BrdU continuously for 8 days to label in vivo as many proliferating cells as possible (1^{st} label). After a short interval, mice were then administered the other nucleotide analog, EdU, for pulse labeling (2^{nd} label) (**Figure 28**A). The rationale for this consecutive and double labeling experiment is as follows. If BECs can be classified into two distinct states, actively and continuously dividing state and quiescent state, then those that are subjected to the 2^{nd} labeling (corresponding to the actively and continuously dividing cells) should have also undergone the 1^{st} labeling and are mostly observed as the 1^{st} and 2^{nd} label double-positive population. Conversely, if BECs are able to convert between the proliferative and quiescent states reversibly, they can divide at arbitrary time points and hence the 1^{st} and 2^{nd} labeling occur independently. In this case, significant numbers of the 2^{nd} label single positive cells should be observed (**Figure 28**B). This experimental strategy can thus allow me to reveal the mode of cell proliferation in terms of their short-term transition between the proliferative and quiescent states. I have to note that the definition of proliferative capacity in this particular set of experiments is based on the relatively short-term cell behavior, and the proliferative or quiescent state of a current cell does not apply to its progeny. In other words, BECs are classified by their transient cell division manner, though they are not restricted to this state permanently.

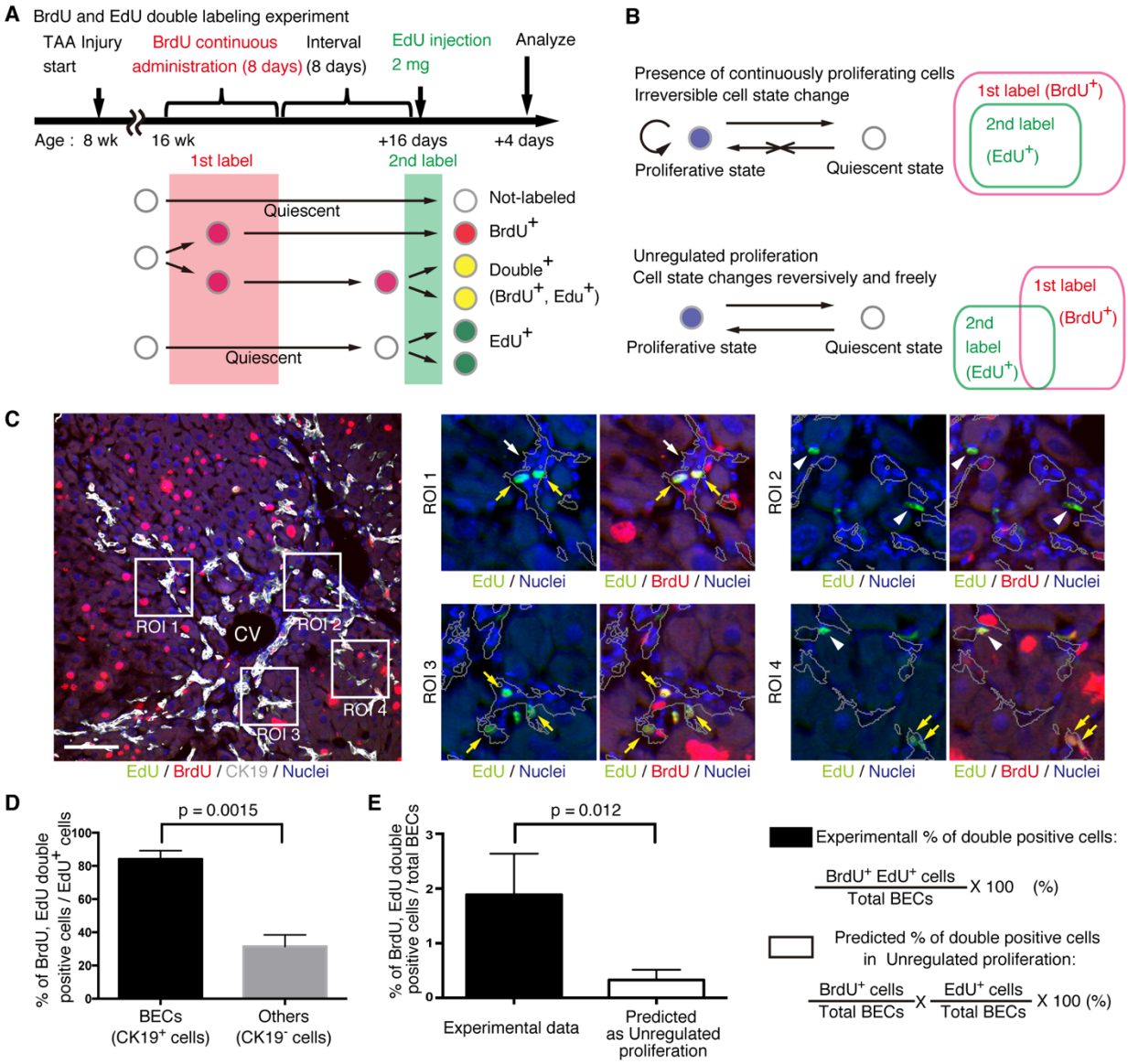

Figure 28. BECs do not proliferate uniformly and can be subdivided into those in the proliferative state and those in the quiescent state. (**A**) Schematic diagram for the experimental design. At 8 weeks of the TAA injury model, mice were given BrdU via drinking water (0.8 mg/ml) for 8 days (1st label). After an interval of a further 8 days, the mice were intraperitoneally injected with EdU (2 mg/20 g body weight) for pulse labeling (2nd label). (**B**) Schematic diagram depicting two possible growth modes. In the top model, proliferative and quiescent cell populations can be distinguished by temporal state. This growth mode will give an experimental result in which the 2nd label+ cells are included within the 1st label+ cells. In the second model (bottom), the cells change their growth state in an unregulated manner, resulting in an un-biased labeling pattern. (**C**) Immunofluorescent staining results for BrdU and EdU incorporation together with CK19 immunostaining. Representative regions of interest (ROI 1-4) in the left panel are shown in the middle and right

panels. In the magnified images, the boundaries of the $CK19^+$ areas are delineated in gray lines. White arrowheads, EdU^+ $BrdU^-$ cells; white arrows, non-labeled cells; yellow arrows, $BrdU^+$ EdU^+double-positive cells. Scale bar represents 100 μm. (**D**) Quantification of the $BrdU^+$ EdU^+ double-labeled cells. Data represents the mean ± SEM for 5 mice. (**E**) Comparison of the incidence of the $BrdU^+$ EdU^+ cells between the experimentally obtained data and the result predicted by the assumption that the BrdU and EdU labeling occur independently. p-value was calculated by two-tailed paired Student's t-test. All experiments were performed with 5 biological replicates.

I observed many BrdU and EdU double positive cells located in the biliary tissue structure, which constituted the major part of the EdU-labeled BEC population (**Figure 28**C, D). In contrast, the majority of the EdU^+ cells were $BrdU^-$ among non-BEC (CK19) populations, confirming that the presence of the double positive cells was not attributable to insufficient washout of the 1^{st} label. I also compared the proportion of the double positive BECs that were experimentally obtained, with the one theoretically predicted from the amount of each labeled populations assuming that BECs proliferate in an unregulated manner (**Figure 28**B, lower panel), and found that their difference was statistically significant (**Figure 28**E). These results suggest that the proliferation pattern of BECs conforms more closely to the model where BECs can take two different states and change from one to the other irreversibly (**Figure 28**B, upper panel).

A stochastic model explains the proliferation dynamics of BECs in vivo.

By combining the data for quantitative single cell tracing (**Figure 23**) and the short-term proliferation behavior (**Figure 28**), I finally sought to establish a mathematical model that can explain the dynamics of the biliary epithelial tissue growth in vivo. In the fitting process for a putative tissue growth model, computational simulation by the Markov chain Monte Carlo methods was employed using R software to obtain numerous outputs for different sizes of BEC colonies, which eventually converged into a specific distribution pattern. Many rounds of simulation, validation, and modification of different parameters in various combinations were performed until I obtained a result of simulation that fitted well with the empirical data from clonal tracing in vivo (See Materials and methods for details).

Considering the results of nucleotide double labeling experiments (**Figure 28**), I assumed a simple growth model driven by two cell states, continuously proliferating cells and quiescent cells. As stated before, I recognized that the most distinctive feature of the quantitative clonal tracing data was the heterogeneity in BECs with regard to the proliferative activity, as manifested by uni-modality and long-tailed pattern of the colony size distribution (**Figure 23**G and I). To construct a model that recapitulates this feature, I hypothesized that there must be a factor that account for heterogeneous proliferative capacities of each cells. Thus, I incorporated a stochastic cell behavior into this two-state growth model, in that a cell in the proliferative state can alter its growth state to

the quiescent state in a probabilistic manner (**Figure 29**A). The term "stochastic" herein is used in exactly the same manner as in previous studies (Doupé et al., 2010; Driessens et al., 2012) and to describe that the state of each cell is unpredictable, rather than being fixed or pre-determined, with total proportion of each divergence being balanced. It is important to note that the concept of stochastic growth does not mean that the process occurs in a non-regulated manner. There are factors that indeed regulate the cellular growth state and behavior, while switching and maintenance of each cell state, timing of each cell division, and duration of each cell cycle "appear" as stochastic. Such stochastic behavior has already been shown to exist in progenitor cells in the inter-folliculer epidermis (IFE) (Doupé et al., 2010; Driessens et al., 2012) and I defined parameters based on that IFE model (**Figure 29**A). As expected, the model with the stochastic feature produced a widespread colony size distribution, with each single proliferating cells yielding colonies with various sizes along time course (**Figure 29**B).

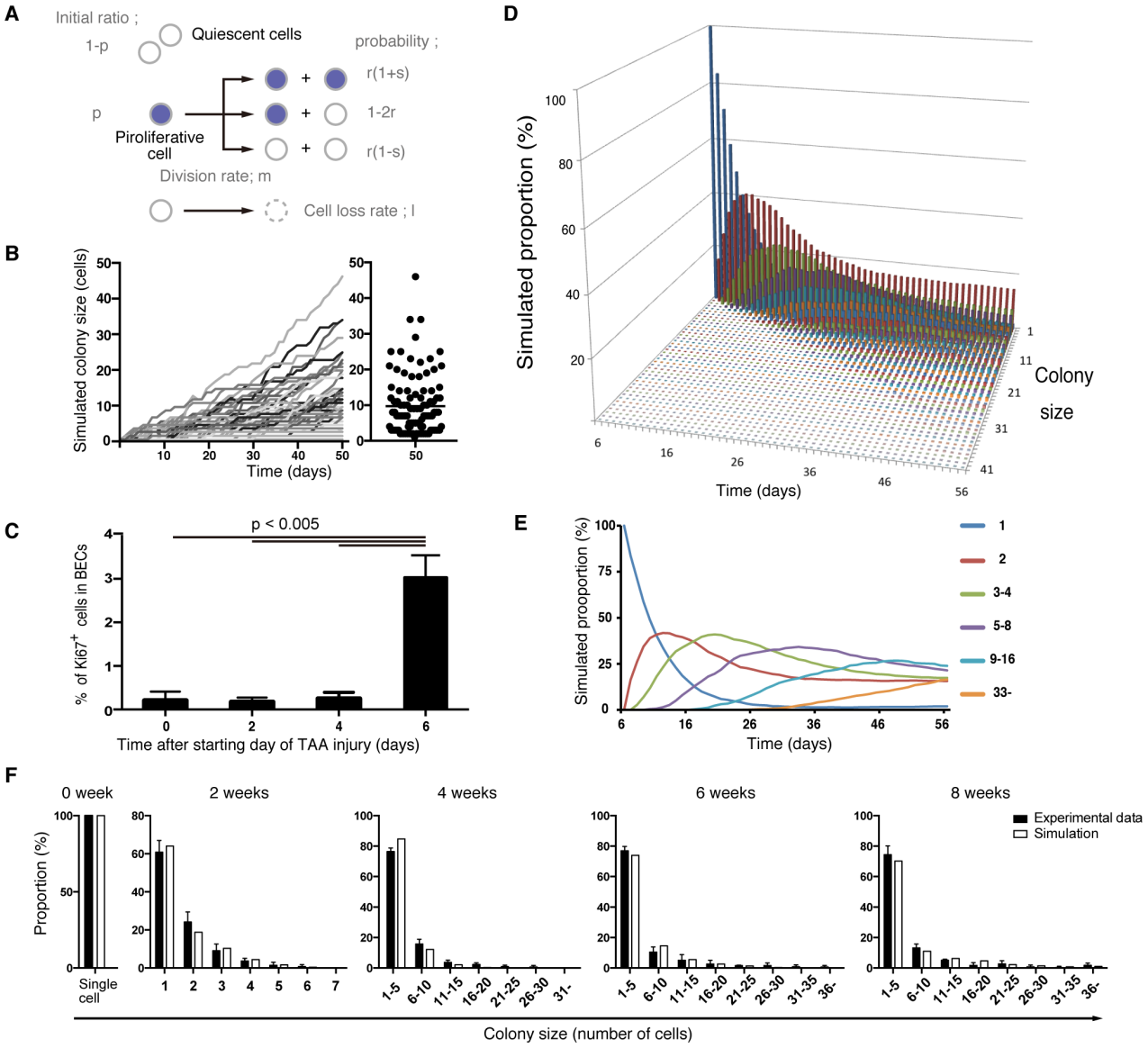

Figure 29. Mathematical modeling predicts the stochastic nature of the BEC proliferation. (**A**) Schematic diagram of the proposed growth model. I set five parameters. The parameter p represents the initial ratio of the cells in the proliferative state compared to total cells; m represents the probability that a cell will enter the cell cycle within one day. The frequency of each cell fate is defined by two parameters, r and s: r affects stability of colony size, whereas s represents imbalance of cell fate selection between proliferative and quiescent states. l represents the probability that a cell will be lost due to cell death (expressed as lost cells per total number of cells per day). (**B-E**) Monte Carlo simulation was performed using R software. (**B**) Consecutive changes in colony size over time are shown in the graph on the left. Each line represents a colony derived from a single proliferative cell. The scatter plot on the right corresponds to the colony-size distribution after 50 days of growth. (**C**) Quantitative data for Ki67^{+} BECs upon TAA injury revealed by immunostaining.

Day 0 samples correspond to livers under normal conditions. A significant increase in $Ki67^+$ cells among the BEC population was observed between 4 and 6 days after the start of injury ($p<0.005$, two-tailed paired Student's t-test). Data represent mean ± SEM for 4 mice. (**D** and **E**) A simulated pattern for distribution of colony size and changes in this distribution for colonies derived from a single proliferative cell. Results are shown for a simulation when the parameters were set as follows: $m = 0.175$, $r = 0.15$, $s = 0.06$, and $l = 0.001$ (simulated cell number = 2000). (**F**) The quantified in vivo data alongside simulation results. The data simulating changes in colony size were constructed from the data for a single proliferative cell (**D** and **E**) compensated for the presence of quiescent cells (the initial ratio $p = 0.465$).

During the model fitting process, the overall result of simulation could almost adequately fit the experimental in vivo clonal tracing data, but I nevertheless encountered an inevitable discordance between them specifically at the time point of 2-week injury (**Figure 30**). I found that a result of simulation for 8-day injury period fitted significantly better with the experimental data for 2-week tracing, implying a gap of several days between the timing of colony formation in vivo and in silico. The initial simulation model I had used up until this point was built based on the assumption that the BECs started entering the proliferative mode on the same day when the injury was induced. I reasoned that the gap might be due to the incorrect estimation of the timing for commencement of BEC proliferation upon injury, as there must be a lag between the timing of the injury application and of the concomitant induction of tissue growth. To test this hypothesis, I performed additional immunostaining experiments using Ki67 and found that BECs first entered the cell cycle in vivo 6 days after the TAA injury was started (**Figure 29**C). This result was consistent with my prediction and I modified the parameter for the starting point in the revised simulation model accordingly. This modification rendered the obtained patterns of simulation to completely fit the experimentally obtained in vivo data over the time course examined (**Figure 29**D-F).

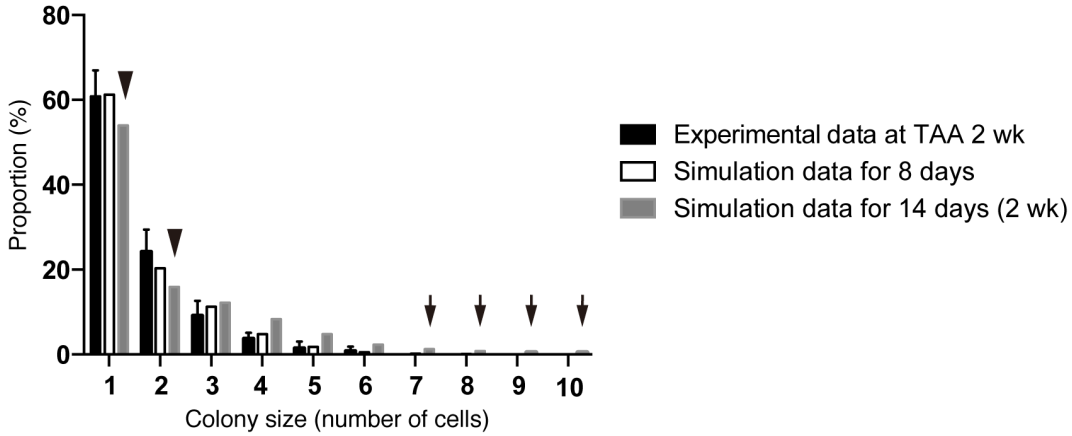

Figure 30. Discordance observed during the model-fitting process before taking account of the timing of the start of BEC proliferation upon injury. Simulation data obtained from a model that is not adjusted for the proliferation start timing (gray bars) did not fit the experimental data for BEC colony formation in vivo (black bars). Early in the model-fitting process, the optimum model with the parameters set to best fit the data for colony-size distributions at 4, 6 and 8 weeks of injury showed a considerable discrepancy in fitting the data for 2 weeks of injury (black arrowheads and arrows). In particular, relatively large colonies were found only in the simulation data (black arrows). Simulated data for 8 days of injury, albeit using the same model and parameters (white bars), showed better fit with the experimental data for 2 weeks of injury than did simulated data for 2 weeks of injury.

I further evaluated my model by an additional experiment. My model predicted that the rate of "cell loss" should be minimal in the BEC population (model parameter l = 0.001, this means only 0.1 % of BECs would be lost in a day). I evaluated the occurrence of cell death in TAA injury by an in vivo cell death detection method (Edwards et al., 2007). As expected, almost no cell death was detected in the $CK19^{+}$ area (**Figure 31**), thus supporting my model prediction.

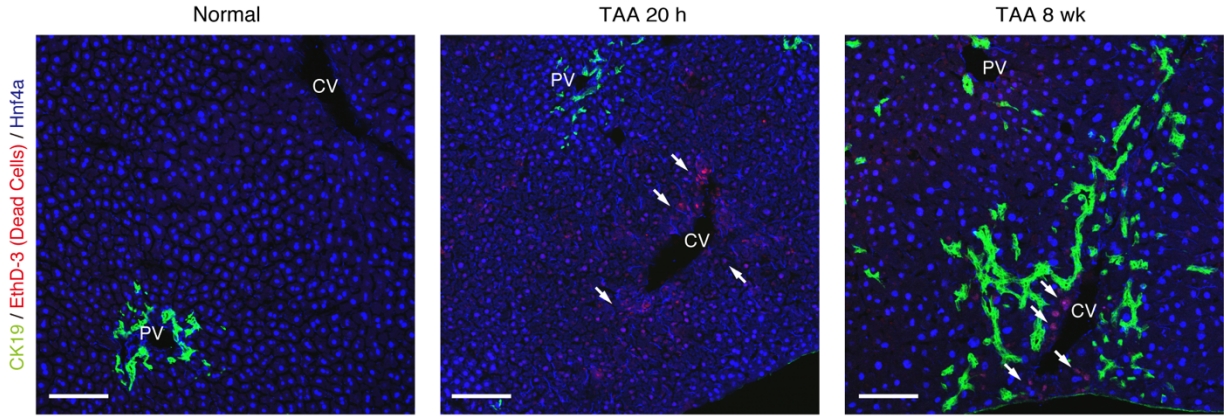

Figure 31. TAA causes death of hepatocytes around CV, but not death of BECs. in vivo cell death detection assay. BECs and hepatocytes were visualized with CK19-antibody and Hnf4A-antibody respectively. Scale bar indicates 100 μm. White arrows show nuclei of dead cells, which incorporated EtD-3. All EthD-3 signal was found in $Hnf4A^{+}$ nuclei, meaning that TAA induce cell death in the hepatocytes specific manner.

Taken together, these results strongly suggest that the proliferation dynamics of BECs upon TAA injury conforms to the following stochastic model: (i) upon liver injury, some BECs are activated to change their growth state to the proliferative state, while the others remain quiescent; (ii) those BECs that are in the proliferative state can stochastically and irreversibly convert back to the quiescent state during the course of injury; (iii) highly proliferative BEC subpopulation is stochastically maintained and produces a large number of progenies, thereby making a major contribution to the biliary epithelial tissue expansion and remodeling.

Discussion

Understanding the relationship between the mode of cell proliferation and the resultant structural organization within a tissue is one of the fundamental issues in stem cell biology. Here, I sought to reveal this relationship by focusing on DR, a unique and dynamic remodeling process of the intrahepatic biliary tree upon chronic liver injury. My results have delineated a progressing morphological transformation of the peripheral ductular structure in the TAA model, which is primarily achieved by a tissue-intrinsic cell expansion within the pre-existing biliary epithelium. Intriguingly, biliary epithelial tissue expansion is dictated by heterogeneous and stochastic behavior of BECs. Thus, a subset of proliferating BECs that is stochastically maintained, rather than a pre-determined and hard-wired progenitor population, exhibits clonogenic growth potential in vivo and plays a central role in the biliary epithelial tissue remodeling.

In the present and recent studies, our laboratory has collectively shown that the biliary epithelial tissue comprises of clearly distinct structural units (**Figure 13**B, C) (Kaneko et al., 2015). In many instances, the architecture of the biliary tree is illustrated as a simple monolayer tube with a luminal structure corresponding to the ducts, with little or no attention being paid to the presence of peripheral ductules. However, it is the ductule compartment, rather than the ducts, that makes a key contribution to tissue remodeling, as indicated by the fact that the majority of the proliferating BECs reside in the peripheral ductule region (**Figure 23**G and **Figure 25**). Structural and functional units found in many different organs, such as the intestinal crypt and the hair follicle, exhibit fairly ordered structure in that they are reiteratively aligned in quasi-two-dimensional sheet-like tissue structures. In contrast, the biliary tree, especially the ductule compartment, spreads omni-directionally and it is quite difficult to capture its structure comprehensively and reproducibly. Therefore, it is necessary to use 3D imaging methods when one need to capture the tissue structures and cellular growth dynamics therein accurately and precisely. In order to observe detailed features and connectivity within the biliary tree structure in the liver, I have established a novel 3D staining and imaging method. It is of notable advantage for the method to be performed easily and effectively with minimum time and cost, especially for those experiments where numerous numbers of samples should be handled, such as the case for the quantitative single cell tracing analysis. I have thoroughly optimized the 3D imaging protocol at various steps to render it easy and cost-

effective without the need for expensive reagents or specialized equipment. The protocol should thus be of versatile use for studying various tissue structures in the liver, as well as in other organs.

Using the quantitative single cell tracing, I have revealed cellular heterogeneity in the biliary epithelial tissue in vivo. More specifically, I found two levels of heterogeneity among the BEC population. Firstly, the biliary epithelial tissue can be subdivided into two classes based on the morphological and geographical characteristics, namely the duct and peripheral ductule compartments. At the population level, the BECs in the latter compartment have higher proliferative capacity than those in the former (**Figure 23**G and **Figure 25**). Secondly, among the BECs in the peripheral ductule compartment, there exists further heterogeneity in terms of the proliferative behavior. Not all the ductule cells exhibit proliferative response upon injury, and the size of the colonies varies even among the proliferative population. Both of these levels of heterogeneity can be explained by my mathematical model. The model predicts the initial ratio of proliferating BEC population to be $p=0.465$, meaning that the majority of BECs do not divide in response to the injury stimulus. This is consistent with the notion that the duct compartment cells, which constitute the major part of the BEC population under the normal condition, do not or rarely divide upon injury (**Figure 25**). The proliferative heterogeneity in the peripheral ductule compartment is well represented as the feature of stochastic growth state change (i.e., proliferating vs. non-proliferating states) of BECs.

I showed that the proliferative state of BECs switched irreversibly to a quiescent state by the dual nucleotide labeling experiment (Figure 6). This feature has also been reported in a previous study about epithelial tissue in vivo (Doupé et al., 2010; Driessens et al., 2012), but is not consistent with a report that studied cell division manner and cell fate decision using an in vitro model (Spencer et al., 2013). I think the discrepancy may be due to the role of BECs in vivo. During the remodeling and growth process of the biliary epithelial tissue, BECs must form a functional tubular structure. I assume that BECs may gain a type of steady-state phenotype (or, become more matured and differentiated cells) in order to generate and maintain a functional and robust epithelial tubular structure. From this point of view, it is reasonable to assume that proliferation state changes irreversibly in vivo. Unfortunately, there is no established marker so far that can clearly distinguish different stages of BECs in the course of their functional differentiation and maturation, which

prevented me from directly evaluating this possibility. Nevertheless, it could be supported in part by the findings that revealed the relationship between the proliferative capacity of BECs and structural feature of the biliary tree (**Figure 23**G), as BECs constituting different tissue structures may be in distinct differentiation stages.

The opposing concepts of "stochastic" versus "deterministic" cell fate decision models have been established as an important paradigm in stem cell biology (Enver et al., 2009; O'Neill and Schaffer, 2004). It should be noted that the concept of stochastic/deterministic regulation, which is concerned in **Figure 23** and **Figure 29**, does not refute the existence of temporal proliferative sub-states, as shown in the dual nucleotide labeling experiment (**Figure 28**). Here, the deterministic model refers to restriction of the cell to a state that is permanently fixed. In both models, cells are divided into sub populations according to their transient proliferative state, rather than permanent state. Thus, the existence of proliferative state does not refute the stochastic model, and the existence of temporal proliferative state does not simply mean the deterministic model. However, the mechanisms governing maintenance and regulation of these cells are defined differently. In the stochastic model, for example, tissue stem cells have non-uniform cell fate and the consequences are not predictable, while in the deterministic model, the stem cells give rise to their progeny uniformly and stably. The concept of the stochastic growth model first emerged in the 1960s, in order to explain the heterogeneous behavior of transplanted hematopoietic stem cells (Siminovitch et al., 1963; Till et al., 1964). Since then, many studies have revealed the existence and role of stochastic feature in various phenomena in organisms (Samoilov et al., 2006). Not only in the cell fate decision process as mentioned above, I also took stochastic feature in the cell cycle length regulation into the simulation (**Figure 29**). In the computational simulation, I defined quiescent cells as those that do not divide at all, avoiding to consider their cell cycle length. On the other hand, the cell cycle length of proliferative cells had to be considered. I first ran many simulations with a uniform cell cycle length for all cells. I found, however, that the best fit was achieved only when a variation of cell cycle length among the cells was considered. The variation was defined as the parameter m (See Methods for details). Interestingly, this result agrees with the notion proposed by Spencer et al., (Spencer et al., 2013), which confirmed by their single cell experimental system that there is a large cell-to-cell variation of cell cycles and delay between mitogen re-

stimulation and CDK activation. They also reported that the cells had heterogeneous inter-mitotic times ranging from 20 hours to > 50 hours. This fits well with my stochastic proliferation model because various inter-mitotic times was considered in our model.

In the concept of the stochastic model, the number and state of stem cells are maintained unstably. This fits considerably well with the structural feature of the biliary tree in many points. First, the biliary tree forms numerous branch ends around the injured area along with injury progression (**Figure 13**E-H, **Figure 15**). In addition, the location of cycling cells appeared to be scattered at the 3D level (**Figure 25**, **Figure 26**). Such frequent remodeling and sporadic proliferation are well suited with the growth model that can maintain proliferating cells to be spatiotemporally flexible. Second, the model is consistent with tissue structural diversity in the micro scale. In microscopic view, the stochastic system shows a degree of instability because the cell state may fluctuate and the output may be unpredictable. This feature well explains the dynamics of the biliary remodeling, in that the detailed shape and degree of expansion of the extended biliary tree varies in each small area of interest (**Figure 13**H). This is why the architecture of the biliary tree looks complicated when observed by 2D liver section. Thus, the instability shown in the stochastic model matches the microscopic structural diversity of the biliary tree. Thirdly, I focused on a feature in the macroscopic scale. In the stochastic model, each cell behaves in a flexible manner, but total percentages of cell fate decision were strictly followed a particular value at the population level (**Figure 29**). This feature of stochastic model makes the simulation outcome converge into an ordered pattern (**Figure 29**C). In other words, the stochastic growth mode provides stable, robust and consistent outcome in a macroscopic view. This macroscopic feature corresponds to the biliary tree architecture in the macroscopic view, as the biliary tree appears to follow a uniform pattern at both the spatial and temporal levels when it is observed in large scale (**Figure 15**).

In conclusion, the stochastic behavior of BECs plays a fundamental role in establishing a flexible and adaptive tissue remodeling system in the biliary epithelium, which underlies robust regenerative capacity of the liver upon injury. Studies in other systems including the hematopoietic stem cells and the epidermal homeostasis have also observed similar models and concepts (Doupé et al., 2010; Siminovitch et al., 1963), implying a common and fundamental mechanism that governs stochastic cell behavior. The knowledge on the mode of tissue growth provided by this

study is not limited to the hepatobiliary system, but should also provide significant insights regarding tissue dynamics and homeostasis in many other organs.

Materials and methods

Animal experiments

All animal experiments were conducted in accordance with the Guideline for the Care and Use of Laboratory Animals of the University of Tokyo, under the approval of the Institutional Animal Care and Use Committee of Institute of Molecular and Cellular Biosciences, The University of Tokyo (approval numbers 2501, 2501-1, 2609 and 2706). Prom1-CreERT2 knock-in mice (Zhu et al., 2009) and R26R-tdTomato reporter mice (Madisen et al., 2010) were purchased from Jackson Laboratory and maintained on a C57BL/6J background. Wild-type C57BL/6J mice were purchased from CLEA Japan. 6 to 10 week old mice including both males and females were used unless otherwise specified.

For liver injury models, mice were administered with 0.3 % (wt/vol) TAA in drinking water or fed 0.1 % 3,5-diethoxycarbonyl-1,4-dihydrocollidine (DDC) containing diet. Tamoxifen was dissolved in corn oil and administered via oral gavage. In labeling experiments with nucleotide analogs, BrdU was administered via drinking water (0.8 mg/ml) and EdU via intra-peritoneal injection for pulse labeling.

For the hepatocyte labeling experiment, rAAV2/8-iCre was packaged in HEK293 cells as previously described (Kok et al., 2013). Virus production was performed by Dr. Kok. The iCe expressing plasmid vector was constructed by replacing the GFP insert in the pAM-LSP1-eGFP vector with the iCre gene. iCre was taken from pDIRE, that was a gift from Rolf Zeller (Addgene plasmid # 26745, (Osterwalder et al., 2010). The titered rAAV2/8-iCre was injected by intraperitoneal injection ($1x10^{11}$ vector genome / mice).

Fluorescence activated cell sorting (FACS)

Liver cell preparation and FACS analyses were done as previously described (Okabe et al., 2009). Non-parenchymal cells were obtained from the mouse liver by two-step collagenase liver digestion method and used for FACS analysis. Mice were laparotomized under isoflurane inhalation anesthesia, and 15 ml of pre-warmed (at 37 ˚C) Liver Perfusion Medium (17701-038, Life technologies) was perfused through the liver from the portal vein. The liver was then perfused with

20 ml of collagenase solution containing collagenase type IV (C5138-5G, Sigma Aldrich) and fetal bovine serum (FBS, S1820-500, Biowest). The liver was harvested and placed into Dulbecco's Modified Eagle Medium (D5796, Life technologies) after removing the gallbladder and extra-hepatic bile duct, and minced gently with surgical knives. Roughly digested liver samples were filtered through a cell strainer (70 μm). The remaining undigested clots were further treated with digestion solution containing collagenase type IV, DNase I (DN25-5G, Sigma Aldrich), and pronase (10165921001, Roche). After removing the parenchymal fraction (hepatocytes) by centrifugation, the non-parenchymal fraction in the supernatant was treated with hemolysis buffer to remove red blood cells. The remaining cells were incubated with anti-FcR antibody, followed by staining with antibodies listed in Table 1. Stained cells were suspended in phosphate-buffered saline (PBS) containing 3 % FBS and 4',6-diamidino-2-phenylindole (DAPI, D3571, Life technologies) for dead cell staining.

In the EdU uptake experiments, I used Click-iT Plus EdU Alexa Fluor 647 Flow Cytometry Assay Kit (C10634, Life technologies) and Fixable Viability Stain 450 (562247, BD Biosciences) according to the manufacturers' instructions.

Data were acquired using FACS Canto II cell analyzer (BD Biosciences) or MoFlo XDP (Beckman Coulter). Final data analyses were performed with FlowJo software.

Table 1. List of antibodies used in this study (Chapter 1)

Antibody	Company/Source	Host animal	Method	Dilution
Prom1/CD133 (APC-conjugated)	Biolegend	rat	FACS	1:200
Prom1/CD133 (purified)	eBioscience	rat	IF	1:200
EpCAM (FITC-conjugated)	(Okabe et al., 2009)	rat	FACS	1:200
EpCAM (purified)	BD Pharmingen	rat	IF	1:200
CD45 (APC-conjugated or APC-Cy7-conjugated)	Biolegend	rat	FACS	1:200
MIC1-1C3	STEMGENT	rat	FACS	1:200
Spp1	R&D systems	goat	IF	1:200
CK19	(Tanimizu et al., 2003)	rabbiy	IF	1:2000
Ki67	eBioscience	rat	IF	1:200
LacZ	Abcam	chicken	IF	1:200
BrdU	Abcam	rat	IF	1:200
Hnf4A	Santa cruz	goat	IF	1:200

Imaging methods

Immunohistochemistry of liver section (2-D Immunohistochemistry)

Whole liver samples from adult mice were fixed with paraformaldehyde (PFA) as follows. The liver was perfused via the portal vein sequentially with 10 ml of PBS, 10 ml of 2 % PFA, and 10 ml of 4 % PFA. Upon harvest, the liver was cut into several blocks, placed into a 15 ml tube containing 4 % PFA, and incubated for 12 hours. After fixation, the liquid was changed to 20 % sucrose in PBS. The liver blocks were embedded in Tissue-Tek O.C.T. compound (Sakura Finetek) and snap frozen. Frozen samples were cut into 10-um thickness using cryostat-microtome (HM525, Microm International) and stained with antibodies described in Table 1. For BrdU immunodetection, sections were heat-treated in TE buffer in an autoclave (120 °C, 5 min) for antigen retrieval. For EdU detection, sections were treated with Click-iT Plus EdU Alexa Fluor 488 Imaging Kit (C10637, Life technologies). Nuclei were counterstained with Hoechst33342 (H1399, Life technologies).

Immunohistochemistry of thick liver section (3D Immunohistochemistry)

The mouse liver samples were pre-fixed using the same protocol as described for the conventional 2D staining. Note that the fixation steps by perfusion were essential to keep the tissue structure intact and to prevent soluble proteins from leaking out. The frozen liver samples were cut into thick sections with 200-500 um thickness using the cryostat-microtome. At this point, the samples set on the stage of the microtome were briefly warmed (by touching with gloved fingers) immediately before sectioning to prevent the samples from cracking. Samples were placed in PBS in disposable tubes, washed with PBS two more times, and then incubated with blocking/permeabilization reagent (3 % FBS, 0.02 % sodium azide, and 0.2 % Triton X-100 in PBS) for 30 min at room temperature (RT). The same blocking/permeabilization reagent was also used in the following staining process for antibody dilution. I typically stained 10 thick sections in a 2 ml tube with 500 μl of diluted antibody solution. The samples were incubated in the antibody solution on a rocking or shaking device at 4 ˚C for 2 days. The tubes were inverted by hand once a day to facilitate thorough mixing and uniform staining. The samples were washed with PBS twice and then transferred into a new 50 ml tube with 40 ml of PBS to wash out excess primary antibodies by incubating on a rocking device at 4˚C for 2 days. After thorough washing, samples were treated with fluorescence-

conjugated secondary antibodies in the same manner as for the primary antibody staining process. Nucleotide staining dye such as Hoechst33342 was mixed into the secondary antibody solution if necessary. Samples were then washed thoroughly with PBS again. After staining and washing, samples were treated with the tissue clearing reagent SeeDB (Ke et al., 2013). The SeeDB reagent contains fructose as the main component and is safe, inexpensive, and easy to handle. I compared various different types of clearing reagents and obtained the highest quality in liver tissue imaging with SeeDB.

When quantitative single cell tracing analyses were performed based on the tdTomato fluorescence, I stained liver cell nuclei by treating sectioned samples with SYTOX Green (in PBS containing 0.1% Triton X-100) on a rocking device overnight at RT. The samples were washed once with PBS and then directly placed into SeeDB.

For data acquisition, I used confocal microscopes (FV1000 or FV1200, Olympus) with a 30x silicone immersion lens (UPLSAPO30XS, Olympus).

I classified BECs into two compartments, duct and ductule, based on two criteria. First, location within the biliary tree structure was considered. In injured liver, the duct still goes along with the PV, while the ductule is expanded to the outer parenchymal area. Second, I measured the diameter of the internal luminal space of the biliary structure. Biliary epithelial tubular structures with the luminal diameter being larger than 8 mm were defined as the duct compartment, while the others with smaller diameter as the ductule.

X-gal staining of mouse liver

For organ-wide 3D visualization of the biliary tree, I performed X-gal staining with whole liver samples derived from the Prom1-CreERT2 mice where nLacZ is also knocked-in to the *Prom1* locus. The liver was perfused with 10 ml of ice-cold PBS containing 2 mM $MgCl_2$, followed by 10 ml of fixative solution (0.2 % PFA, 0.1 M HEPES, 2 mM $MgCl_2$, 5 mM EGTA, pH 7.3). The liver was incubated with fixative solution for 48 hours at 4 ˚C with a daily change of the solution. The fixed liver was then treated with detergent buffer (0.1 M phosphate buffer, pH 7.3, 2 mM $MgCl_2$, 0.01 % sodium deoxycholate, 0.02 % Nonidet P-40) for 24 hours at 4 ˚C. Next, the liver was treated with staining buffer (1 mg/ml X-gal in detergent buffer) for 48 hours at 4 ˚C (from this step on, sample

tubes were wrapped with foil for shading) and further for 12 hours at 37 ˚C. At all incubation steps, samples were put on a rocking device. After washing out staining buffer with PBS, the liver was dehydrated with ethanol and then cleared with a 2:1 benzyl benzoate:benzyl alcohol (BABB) solution.

in vivo cell death detection

For evaluation of cell death in injured liver, I performed a cell death detection assay (Edwards et al., 2007) with some modification. 200 μl of EthD-3 (0.2 mg/ml in PBS, PK-CA707-40050, Takara) was injected intravenously to stain nuclei of dead cells in vivo in living mice. After 15 minutes, mice were killed and PBS was perfused via the portal vein to drain the blood that contained excess EthD-3. Then the liver was processed using the 2D staining protocol as described above.

Statistics

In all animal experiments, the samples represent biological replicates derived from different mouse individuals. Representative data were supported by at least three biological replicates. Detailed sample size was estimated by considering the means and variation data of preliminary experiments. No randomization or blinding process was performed.

F-test was used to check homoscedasticity of the data, and Kolmogorov-Smirnov test to check whether the data follow Gaussian distribution. Significance tests were performed as described in legends to each figure using Prism software (Graph pad).

Modeling and simulation

Data acquisition by 3D imaging

To determine the exact number of cells in a clone originating from a single BEC, I had to acquire a detailed 3D image for the entire clone in liver tissues. In many studies, the number of cells in a colony has been calculated or estimated based on the data obtained from 2D sectioned images. For example, in a previous study in which a similar statistical method was employed to reveal the growth mode of the epidermis (Driessens et al., 2012), the number of cells in a clone (clone size) was estimated by 2D section images. This was because the clones formed in the epidermis had an ordered shape and the actual clone size was well correlated with the estimation that can be derived

from 2D section images. In stark contrast, the biliary tree exhibits branching and diversified 3D structures, which become far more complex under the liver injury condition, so that it is practically difficult to estimate the clone size accurately based on 2D section images. Hence, rather than calculating or estimating cell numbers from the 2D section, I chose to perform the 3D imaging followed by directly cell counting to quantify the exact cell number in each colony. This approach is more time consuming than those relying on 2D image analyses, but it can reduce potential experimental errors and artifacts that might occur during the process of the clone size calculation or estimation.

In the quantitative single cell tracing experiments performed in the present study, I analyzed the liver samples by making thick sections with 300 μm thickness. This enabled me to acquire 3D observation of the entire structure of the labeled clones in the biliary tree. I genetically labeled BECs at a very low frequency to perform a single cell tracing. This resulted in extremely low density (or, incidence) of the labeled clones in the liver tissues so that it was necessary to examine and observe vast numbers of samples in order for me to achieve data with enough size. One section of a 300 μm thickness has an equivalent data size to 30 sheets of 10-μm-thick 2D sections. Thus, the 3D imaging not only provided the 3D structural information on clone sizes but also enabled me to survey large areas in tissue samples very efficiently.

As mentioned before, the liver samples were treated with a nucleotide staining reagent SYTOX Green. By counting the number of nuclei in a tdTomato$^+$ colony, I quantified the number of cells in it. It typically took only 10 hours to stain the whole nuclei in thick liver sections with SYTOX Green. Treating the stained tissue with the clearing reagent SeeDB required 3 hours. I was thus able to complete these sample preparation steps within a day, showing that my protocol is suited for 3D observation of large quantities of tissue samples.

Modeling and parameters

I simulated the biliary epithelial tissue growth using computational Markov chain Monte Carlo methods. In the quantitative single cell tracing experiments, the tissue growth up to 8 weeks of TAA injury was analyzed. I thus sought to reproduce the cellular behavior observed during this time course by simulation. I defined the start timing of BEC proliferation to occur in a probabilistic

manner, and presumed that the average cell cycle duration (the period from a start timing of cell division to the next one) was longer than 24 hours. I set a simulation model so that each proliferating cell could choose whether or not to start cell division, based on the cell division rate parameter "m" (probability of cell division / a day).

When a cell enters the cell cycle, it should follow one out of three fate options (**Figure 29**A). The probability for this fate selection was defined with two parameters, "r" and "s". The parameter r affects the stability of the colony size, while the parameter s represents an imbalance of the cell fate selection between the proliferative and quiescent states. In the case where totally balanced tissue growth occurs, such as in the normal maintenance state of the adult epidermis, the proportion of the proliferating and quiescent cells is maintained and the parameter s can be ignored ($s = 0$) (Doupé et al., 2010). In contrast, the parameter s should be considered in the case of the biliary epithelial tissue growth, because the biliary tree was expanding drastically (**Figure 13** and **Figure 15**) and the total cell numbers were not maintained during the process. I also added another parameter, "p", which represented the initial ratio of proliferating cells, as I found that there were many quiescent cells in the BEC population (**Figure 23** and **Figure 27**).

In general, a negative effect, such as the density effect, should be included in simulation when a growth model in a limited space is to be constructed. In the simulation, such a negative effect that could potentially be caused by an overgrowth of BECs was not incorporated. It is true that there must be a limit of BECs' growth as they form a simple epithelial tissue and can only reside and expand within the liver of a certain size. However, within the period of 8 weeks of TAA injury, there still remained an empty space for BECs to grow and expand, and I indeed observed that BECs continued to proliferate along with the entire time course (**Figure 13** and **Figure 15**). Hence, I chose not to designate any parameter regarding the density effect into my simulation. It may become necessary if one simulates the growth of BECs at later time points, such as the process of tumor formation.

Chapter 2: Role of DR in liver regeneration

本章については、５年以内に雑誌等で刊行予定のため、非公開。

Conclusion

In this thesis, the mechanisms of DR and liver regeneration were analyzed from two viewpoints. In Chapter 1, we analyzed them by focusing on the growth of BECs. In Chapter 2, we analyzed them by focusing on the role of DR. These two topics, cell growth and the role of DR had been unclear for a long time. It had been difficult to analyze them partly due to the lack of experimental methods. I sought to develop novel imaging methods to overcome the experimental constraints that made the studies of DR and liver regeneration difficult. With newly developed imaging tools, a growth mode of BECs in liver regeneration process was revealed. Furthermore, a unifying explanation for the role of DR in liver regeneration was proposed by the imaging analysis of DR.

In the study of cell growth, the detailed computational growth model was proposed. This model suggests the existence of stochastic process. The feature of the stochastic process has been reported in the various studies of cell growth, however, the molecular mechanism of them was not revealed yet. Further studies are needed to reveal the mechanism of them.

In Chapter 2,

本章については、５年以内に雑誌等で刊行予定のため、非公開。

References

Barker, N., van Es, J.H., Kuipers, J., Kujala, P., van den Born, M., Cozijnsen, M., Haegebarth, A., Korving, J., Begthel, H., Peters, P.J., et al. (2007). Identification of stem cells in small intestine and colon by marker gene Lgr5. Nature *449*, 1003–1007.

Barker, N., Huch, M., Kujala, P., van de Wetering, M., Snippert, H.J., van Es, J.H., Sato, T., Stange, D.E., Begthel, H., van den Born, M., et al. (2010). Lgr5(+ve) stem cells drive self-renewal in the stomach and build long-lived gastric units in vitro. Cell Stem Cell *6*, 25–36.

Branda, C.S., and Dymecki, S.M. (2004). Talking about a revolution: The impact of site-specific recombinases on genetic analyses in mice. Developmental Cell *6*, 7–28.

Cong, L., Ran, F.A., Cox, D., Lin, S., Barretto, R., Habib, N., Hsu, P.D., Wu, X., Jiang, W., Marraffini, L. a, et al. (2013). Multiplex genome engineering using CRISPR/Cas systems. Science *339*, 819–823.

Dorrell, C., Erker, L., Schug, J., Kopp, J.L., Canaday, P.S., Fox, A.J., Smirnova, O., Duncan, A.W., Finegold, M.J., Sander, M., et al. (2011). Prospective isolation of a bipotential clonogenic liver progenitor cell in adult mice. Genes & Development *25*, 1193–1203.

Doupé, D.P., Klein, A.M., Simons, B.D., and Jones, P.H. (2010). The ordered architecture of murine ear epidermis is maintained by progenitor cells with random fate. Developmental Cell *18*, 317–323.

Driessens, G., Beck, B., Caauwe, A., Simons, B.D., and Blanpain, C. (2012). Defining the mode of tumour growth by clonal analysis. Nature *488*, 527–530.

Edwards, J.R., Diamantakos, E.A., Peuler, J.D., Lamar, P.C., and Prozialeck, W.C. (2007). A novel method for the evaluation of proximal tubule epithelial cellular necrosis in the intact rat kidney using ethidium homodimer. BMC Physiology *7*, 1.

Enver, T., Pera, M., Peterson, C., and Andrews, P.W. (2009). Stem cell states, fates, and the rules of attraction. Cell Stem Cell *4*, 387–397.

Español-Suñer, R., Carpentier, R., Van Hul, N., Legry, V., Achouri, Y., Cordi, S., Jacquemin, P., Lemaigre, F., and Leclercq, I. a (2012). Liver progenitor cells yield functional hepatocytes in response to chronic liver injury in mice. Gastroenterology *143*, 1564–1575.

Etzrodt, M., Endele, M., and Schroeder, T. (2014). Quantitative single-cell approaches to stem cell research. Cell Stem Cell *15*, 546–558.

Fickert, P., Stöger, U., Fuchsbichler, A., Moustafa, T., Marschall, H.-U., Weiglein, A.H., Tsybrovskyy, O., Jaeschke, H., Zatloukal, K., Denk, H., et al. (2007). A new xenobiotic-induced mouse model of sclerosing cholangitis and biliary fibrosis. The American Journal of Pathology *171*, 525–536.

Forbes, S.J., and Newsome, P.N. (2016). Liver regeneration - mechanisms and models to clinical application. Nature Reviews. Gastroenterology & Hepatology *13*, 473–485.

Gouw, A.S.H., Clouston, A.D., and Theise, N.D. (2011). DRs in human liver: diversity at the interface. Hepatology *54*, 1853–1863.

Grompe, M. (2014). Liver stem cells, where art thou? Cell Stem Cell.

Grompe, M., Duncan, A.W., and Dorrell, C. (2009). Stem Cells and Liver Regeneration. Gastroenterology *137*, 466–481.

Hara, K., Nakagawa, T., Enomoto, H., Suzuki, M., Yamamoto, M., Simons, B.D., and Yoshida, S. (2014). Mouse spermatogenic stem cells continually interconvert between equipotent singly isolated and syncytial states. Cell Stem Cell *14*, 658–672.

Hsu, Y.-C. (2015). Theory and Practice of Lineage Tracing. Stem Cells *33*, 3197–3204.

Ishii, T., and Ishii, M. (2011). Intravital two-photon imaging: a versatile tool for dissecting the immune system. Annals of the Rheumatic Diseases *70 Suppl 1*, NaN – NaN.

Ishikawa, T., Factor, V.M., Marquardt, J.U., Raggi, C., Seo, D., Kitade, M., Conner, E.A., and Thorgeirsson, S.S. (2012). Hepatocyte growth factor/c-met signaling is required for stem-cell-mediated liver regeneration in mice. Hepatology *55*, 1215–1226.

Jenne, C.N., Wong, C.H.Y., Petri, B., Chrobok, N.L., and Kubes, P. (2013). Nucleation of platelets with blood-borne pathogens on Kupffer cells precedes other innate immunity and contributes to bacterial clearance. Nature Immunology *14*, 785–792.

Kamimoto, K., Kaneko, K., Kok, C., Okada, H., and Miyajima, A. (2016). Heterogeneity and stochastic growth regulation of biliary epithelial cells dictate dynamic epithelial tissue remodeling. eLife.

Kaneko, K., Kamimoto, K., Miyajima, A., and Itoh, T. (2015). Adaptive remodeling of the biliary architecture underlies liver homeostasis. Hepatology *61*, 2056–2066.

Ke, M.-T., Fujimoto, S., and Imai, T. (2013). SeeDB: a simple and morphology-preserving optical clearing agent for neuronal circuit reconstruction. Nature Neuroscience *16*, 1154–1161.

Kellogg, R.A., and Tay, S. (2015). Noise Facilitates Transcriptional Control under Dynamic Inputs. Cell *160*, 381–392.

Kikuchi, S., Hata, M., Fukumoto, K., Yamane, Y., and Matsui, T. (2002). Radixin deficiency causes conjugated hyperbilirubinemia with loss of Mrp2 from bile canalicular membranes. Nature *31*, 320–325.

Kok, C.Y., Cunningham, S.C., Carpenter, K.H., Dane, A.P., Siew, S.M., Logan, G.J., Kuchel, P.W., and Alexander, I.E. (2013). Adeno-associated virus-mediated rescue of neonatal lethality in argininosuccinate synthetase-deficient mice. Molecular Therapy : The Journal of the American Society of Gene Therapy *21*, 1823–1831.

Kretzschmar, K., and Watt, F.M. (2012). Lineage Tracing. Cell *148*, 33–45.

Lu, W., Bird, T.G., Boulter, L., Tsuchiya, A., Cole, A.M., Hay, T., Guest, R.V., Wojtacha, D., Man, T.Y., Mackinnon, A., et al. (2015). Hepatic progenitor cells of biliary origin with liver repopulation capacity. Nature Cell Biology *17*, 971–983.

Madisen, L., Zwingman, T. a, Sunkin, S.M., Oh, S.W., Zariwala, H. a, Gu, H., Ng, L.L., Palmiter, R.D., Hawrylycz, M.J., Jones, A.R., et al. (2010). A robust and high-throughput Cre reporting and characterization system for the whole mouse brain. Nature Neuroscience *13*, 133–140.

Michalopoulos, G.K. (2014). The liver is a peculiar organ when it comes to stem cells. The American Journal of Pathology *184*, 1263–1267.

Michalopoulos, G.K., and Khan, Z. (2015). Liver Stem Cells: Experimental Findings and Implications for Human Liver Disease. Gastroenterology *149*, 876–882.

De Minicis, S., Kisseleva, T., Francis, H., Baroni, G.S., Benedetti, A., Brenner, D., Alvaro, D., Alpini, G., and Marzioni, M. (2013). Liver carcinogenesis: rodent models of hepatocarcinoma and cholangiocarcinoma. Digestive and Liver Disease : Official Journal of the Italian Society of Gastroenterology and the Italian Association for the Study of the Liver *45*, 450–459.

Miyajima, A., Tanaka, M., and Itoh, T. (2014). Stem/progenitor cells in liver development, homeostasis, regeneration, and reprogramming. Cell Stem Cell *14*, 561–574.

Miyaoka, Y., and Miyajima, A. (2013). To divide or not to divide: revisiting liver regeneration. Cell Division *8*, 8.

Nagahama, Y., Sone, M., Chen, X., Okada, Y., Yamamoto, M., Xin, B., Matsuo, Y., Komatsu, M., Suzuki, A., Enomoto, K., et al. (2014). Contributions of hepatocytes and bile ductular cells in ductular reactions and remodeling of the biliary system after chronic liver injury. The American Journal of Pathology *184*, 3001–3012.

O'Neill, A., and Schaffer, D.V. (2004). The biology and engineering of stem-cell control. Biotechnology and Applied Biochemistry *40*, 5–16.

Okabe, M., Tsukahara, Y., Tanaka, M., Suzuki, K., Saito, S., Kamiya, Y., Tsujimura, T., Nakamura, K., and Miyajima, A. (2009). Potential hepatic stem cells reside in EpCAM+ cells of normal and injured mouse liver. Development *136*, 1951–1960.

Osterwalder, M., Galli, A., Rosen, B., and Skarnes, W.C. (2010). Dual RMCE for efficient re-engineering of mouse mutant alleles. Nature.

Rao, R.K., and Samak, G. (2013). Bile duct epithelial tight junctions and barrier function. 1–10.

Rountree, C.B., Barsky, L., Ge, S., Zhu, J., Senadheera, S., and Crooks, G.M. (2007). A CD133-expressing murine liver oval cell population with bilineage potential. Stem Cells *25*, 2419–2429.

Saleh, M., Kamath, B.M., and Chitayat, D. (2016). Alagille syndrome: clinical perspectives. The Application of Clinical Genetics *9*, 75–82.

Samoilov, M.S., Price, G., and Arkin, A.P. (2006). From fluctuations to phenotypes: the physiology of noise. Science's STKE : Signal Transduction Knowledge Environment *2006*, re17.

Sebesty, M.G., Budker, V.G., Budker, T., Subbotin, V.M., Monahan, S.D., Lewis, D.L., and Wolff, J.A. (2006). Mechanism of plasmid delivery by hydrodynamic tail vein injection . I . Hepatocyte uptake of various molecules. The Journal of Gene Medicine 852–873.

Sebestyén, M.G., Budker, V.G., and Budker, T. (2006). Mechanism of plasmid delivery by hydrodynamic tail vein injection. I. Hepatocyte uptake of various molecules. The Journal of Gene … *8*, 852–873.

Sekiya, S., and Suzuki, A. (2012). Intrahepatic cholangiocarcinoma can arise from Notch-mediated conversion of hepatocytes. *122*, 3914–3918.

Siminovitch, L., McCulloch, E.A., and Till, J.E. (1963). The distribution of colony- forming cells among spleen colonies. Journal of Cellular and Comparative Physiology *62*, 327–336.

Spencer, S.L., Cappell, S.D., Tsai, F.-C., Overton, K.W., Wang, C.L., and Meyer, T. (2013). The proliferation-quiescence decision is controlled by a bifurcation in CDK2 activity at mitotic exit. Cell *155*, 369–383.

Suzuki, A., Sekiya, S., Onishi, M., Oshima, N., Kiyonari, H., Nakauchi, H., and Taniguchi, H. (2008). Flow cytometric isolation and clonal identification of self-renewing bipotent hepatic progenitor cells in adult mouse liver. Hepatology *48*, 1964–1978.

Takase, H.M., Itoh, T., Ino, S., Wang, T., Koji, T., Akira, S., Takikawa, Y., and Miyajima, A. (2013). FGF7 is a functional niche signal required for stimulation of adult liver progenitor cells that support liver regeneration. Genes & Development *27*, 169–181.

Takashima, Y., Terada, M., Kawabata, M., and Suzuki, A. (2015). Dynamic three- dimensional morphogenesis of intrahepatic bile ducts in mouse liver development. Hepatology.

Tanaka, K., Morimoto, Y., Toiyama, Y., Okugawa, Y., Inoue, Y., Uchida, K., Kimura, K., Mizoguchi, A., and Kusunoki, M. (2012). Intravital dual-colored visualization of colorectal liver metastasis in living mice using two photon laser scanning microscopy. Microscopy Research and Technique *75*, 307–315.

Tanaka, M., Itoh, T., Tanimizu, N., and Miyajima, A. (2011). Liver stem/progenitor cells: their characteristics and regulatory mechanisms. Journal of Biochemistry *149*, 231–239.

Tanimizu, N., and Miyajima, A. (2007). Molecular mechanism of liver development and regeneration. International Review of Cytology *259*, 1–48.

Tanimizu, N., Tanimizu, N., Nishikawa, M., Saito, H., Tsujimura, T., and Miyajima, A. (2003). Isolation of hepatoblasts based on the expression of Dlk/Pref-1. Journal of Cell Science *116*, 1775–1786.

Tanimizu, N., Nishikawa, Y., Ichinohe, N., Akiyama, H., and Mitaka, T. (2014). Sry HMG box protein 9-positive (Sox9+) epithelial cell adhesion molecule-negative (EpCAM-) biphenotypic cells derived from hepatocytes are involved in mouse liver regeneration. The Journal of Biological Chemistry *289*, 7589–7598.

Tarlow, B.D., Pelz, C., Naugler, W.E., Wakefield, L., Wilson, E.M., Finegold, M.J., and Grompe, M. (2014a). Bipotential adult liver progenitors are derived from chronically injured mature hepatocytes. Cell Stem Cell *15*, 605–618.

Tarlow, B.D., Finegold, M.J., and Grompe, M. (2014b). Clonal tracing of Sox9+ liver progenitors in mouse oval cell injury. Hepatology *60*, 278–289.

Tay, S., Hughey, J.J., Lee, T.K., Lipniacki, T., Quake, S.R., and Covert, M.W. (2010). Single-cell NF-κB dynamics reveal digital activation and analogue information processing. Nature *466*, 267–271.

Teta, M., Rankin, M.M., Long, S.Y., Stein, G.M., and Kushner, J. a (2007). Growth and regeneration of adult beta cells does not involve specialized progenitors. Developmental Cell *12*, 817–826.

Till, J.E., McCulloch, E.A., and Siminovitch, L. (1964). A STOCHASTIC MODEL OF STEM CELL PROLIFERATION, BASED ON THE GROWTH OF SPLEEN COLONY-FORMING CELLS. Proceedings of the National Academy of Sciences of the United States of America *51*, 29–36.

Wang, H., Yang, H., Shivalila, C.S., Dawlaty, M.M., Cheng, A.W., Zhang, F., and Jaenisch, R. (2013). One-step generation of mice carrying mutations in multiple genes by CRISPR/Cas-mediated genome engineering. Cell *153*, 910–918.

Wang, W., Soroka, C.J., Mennone, A., Rahner, C., Harry, K., Pypaert, M., and Boyer, J.L. (2006). Radixin Is Required to Maintain Apical Canalicular Membrane Structure and Function in Rat Hepatocytes. Gastroenterology *131*, 878–884.

Watanabe, M., Houten, S.M., Wang, L., Moschetta, A., Mangelsdorf, D.J., Heyman, R.A., Moore, D.D., and Auwerx, J. (2004). Bile acids lower triglyceride levels via a pathway involving FXR, SHP, and SREBP-1c. The Journal of Clinical Investigation *113*, 1408–1418.

Williams, a, Elias, E., Cardenas, T., Milkiewicz, P., Cardenas, R., Mills, C.O., and Hubscher, S.G. (2001). Visualization of the transport of primary and secondary bile acids across liver tissue in rats: in vivo study with fluorescent bile acids. *34*, 4–10.

Xue, W., Chen, S., Yin, H., Tammela, T., Papagiannakopoulos, T., Joshi, N.S., Cai, W., Yang, G., Bronson, R., Crowley, D.G., et al. (2014). CRISPR-mediated direct mutation of cancer genes in the mouse liver. Nature *514*, 380–384.

Yang, H., and Duan, Z. (2016). Bile Acids and the Potential Role in Primary Biliary Cirrhosis. Digestion *94*, 145–153.

Yanger, K., Knigin, D., Zong, Y., Maggs, L., Gu, G., Akiyama, H., Pikarsky, E., and Stanger, B.Z. (2014). Adult hepatocytes are generated by self-duplication rather than stem cell differentiation. Cell Stem Cell *15*, 340–349.

Yeh, C.-N., Maitra, A., Lee, K.-F., Jan, Y.-Y., and Chen, M.-F. (2004). Thioacetamide-induced intestinal-type cholangiocarcinoma in rat: an animal model recapitulating the multi-stage progression of human cholangiocarcinoma. Carcinogenesis *25*, 631–636.

Zhu, L., Gibson, P., Currle, D.S., Tong, Y., Richardson, R.J., Bayazitov, I.T., Poppleton, H., Zakharenko, S., Ellison, D.W., and Gilbertson, R.J. (2009). Prominin 1 marks intestinal stem cells that are susceptible to neoplastic transformation. Nature *457*, 603–607.

Acknowledgements

I would like to thank my supervisor, Professor Atsushi Miyajima, and Associate Professor Tohru Itoh for the thoughtful mentoring. I also thank for Naoko Miyata for cell sorting, Noriko Imaizumi for mouse husbandry, the members of the Miyajima lab for discussions and advice. I thank Prof. Ian Alexander (Children's Medical Research Institute, Australia) for the pAM-LSP1-EGFP plasmid, Prof. R Jude Samulski and the NGVB Biorepository (University of North Carolina at Chapel Hill, USA) for the XX6-80 plasmid, Prof. Rolf Zeller for the pDIRE plasmid, and Penn Vector Core (University of Pennsylvania, USA) for the p5E18-VD2/8 plasmid. I thank Graduate Program for Leaders in Life Innovation (GPLLI) and Japanese Society for the Promotion of Science (JSPS) for financial supports.